

Influence of flow thickness on general relativistic low angular momentum accretion around spinning black holes

Pratik Tarafdar^{1*}, Susovan Maity^{2†}, Tapas K. Das^{2‡}

¹S. N. Bose National Centre for Basic Sciences,
Block JD, Sector III, Salt Lake, Kolkata 700 106, India.

²Harish-Chandra Research Institute, HBNI,
Chhatnag Road, Jhunsi, Allahabad 211 109, India.

Abstract

General relativistic, axisymmetric flow of low angular momentum accretion around a Kerr black hole can have certain geometric configuration where the flow is maintained in hydrostatic equilibrium along the vertical direction (direction orthogonal to the equatorial plane of the flow). The flow thickness for such accretion models becomes a function of the local radial distance measured from the black hole horizon. There are three types of functions defined in the literature which resemble the thickness of the flow for such a configuration. We formulate the equations governing the steady state astrophysical accretion characterized by both the polytropic as well as the isothermal equation of state in classical thermodynamics. We solve the equations within the framework of such geometric configuration for three different thickness functions, to obtain the multi-transonic, shocked, stationary integral accretion solutions. Such solutions enable us to study how flow thickness influences the dependence of the properties of post-shock flows on black hole spin angular momentum, i.e., the Kerr parameter. For temperature-preserving standing shocks, we find that the post-shock part of the disc can become luminous and considerable amount of gravitational energy carried by the accreting fluid can get liberated at the shock. We find which kind of thickness function produces the maximum liberated energy, making the disc most luminous.

1 Introduction

Axially symmetric, low angular momentum accretion of hydrodynamic fluid onto astrophysical black holes may exhibit multi-transonic features, and such multi-transonic accretion

*pratika16@gmail.com

†susovanmaity@hri.res.in

‡tapas@hri.res.in

flow is endowed with a stationary shock. Such low angular momentum, practically inviscid flow may be observed in realistic astrophysical systems like detached binaries fed by accretion from OB stellar winds ([Illarionov and Sunyaev, 1975], [Liang and Nolan, 1984]), semi-detached low-mass non-magnetic binary systems ([Bisikalo et al., 1998]), supermassive black holes fed by accretion from weakly rotating central stellar clusters ([Illarionov, 1988], [Ho, 1999] and references therein). For a standard Keplerian accretion flow, various physical processes like turbulence, produce practically inviscid low angular momentum flow (see, e.g. [Igumenshchev and Abramowicz, 1999] and references therein). Several recent works on accretion onto our Galactic Centre black hole indicates the presence of such flow as well ([Melia, 1992], [Melia et al., 2001], [Moscibrodzka et al., 2006], [Moscibrodzka, 2006], [Czerny et al., 2007], [Marrone et al., 2007], [Ghez et al., 2008], [Gillessen et al., 2009], [Ferrière, 2009], [Genzel et al., 2010], [Okuda and Molteni, 2012]).

The multi-transonic features and the formation of the corresponding standing shock have been studied extensively by several authors in the last forty years. Such efforts were initiated for black hole accretion under the influence of the post-Newtonian pseudo-Schwarzschild and pseudo-Kerr potential ([Abramowicz and Zurek, 1981], [Muchotrzeb and Paczynski, 1982], [Fukue, 1983], [Lu, 1985], [Muchotrzeb and Czerny, 1986], [Blaes, 1987], [Chakrabarti, 1989], [Nakayama and Fukue, 1989], [Abramowicz and Kato, 1989], [Abramowicz and Chakrabarti, 1990], [Sponholz and Molteni, 1994], [Bussemaker et al., 1997], [Tóth et al., 1998], [Chakrabarti and Das, 2001], [Das, 2002], [Das et al., 2003], [Okuda et al., 2004], [Fukue, 2004b], [Fukue, 2004a], [Moscibrodzka et al., 2006], [Das and Czerny, 2012], [Saha et al., 2016], [Majumder et al., 2018], [Dihingia et al., 2018]). Eventually, shocked multi-transonic flows have been studied for general relativistic accretion flows as well ([Lu, 1986], [Kafatos and Yang, 1994], [Yang and Kafatos, 1995], [Pariev, 1996], [Nakayama, 1996], [Chakrabarti, 1996], [Chakrabarti, 1996], [Peitz and Appl, 1997], [Fukumara and Tsuruta, 2004], [Barai et al., 2004], [Nagakura and Yamada, 2008], [Nagakura and Yamada, 2009], [Das and Czerny, 2012], [Das et al., 2015], [Suková and Janiuk, 2015], [Suková et al., 2017], [Suková, 2017], [Tarafdar and Das, 2018], [Tarafdar et al., 2019], [Palit et al., 2019], [Dihingia et al., 2019a], [Dihingia et al., 2019b], [Fukue, 2019]), where the work by Fukue ([Fukue, 1983], [Fukue, 1987]) may be attributed to the first ever paper published in the field of study of multi-transonic shocked accretion flow. Of late, such shocked flows have been studied for magneto-hydrodynamic black hole accretions as well ([Takahashi et al., 1992], [Takahashi et al., 2002], [Takahashi, 2002], [Takahashi et al., 2006], [Fukumura et al., 2007], [Sarkar and Das, 2018]).

Geometrical configuration of axisymmetrically accreting fluid can assume three different forms, see e.g., section 4 of [Bilić et al., 2014], for detailed discussions on such configurations. Also see [Chakrabarti and Das, 2001], [Tarafdar et al., 2019] and references therein. In the present work, we concentrate on axially symmetric flows under hydrostatic equilibrium in the vertical direction, where the gravitational force on the accreting fluid is balanced against the fluid pressure force. These commonly used disc models, however, possess certain limitations, and there are certain proposals available in the literature to calculate a more realistic expression for the disc thickness, e.g., [Beskin, 1997], [Hubeny and Hubeny, 1998], [Beskin and Tchekhovskoy, 2005], [Davis and Hubeny, 2006] and [Beskin, 2009]. We, nevertheless, stick to the disc structure maintained in hydrostatic equilibrium along vertical

directions, since dealing with the aforementioned alternate disc models is mathematically very difficult, if not impossible, while obtaining the stationary integral flow solutions from general relativistic Euler and the continuity equations.

First ever detailed calculation of flow structure for general relativistic accretion onto rotating black holes was obtained by Novikov and Thorne (hereafter NT). They provided a particular expression of the disc thickness for flow in hydrostatic equilibrium along the vertical direction ([Novikov and Thorne, 1973]).

Such an expression was slightly modified by Riffert and Herold ([Riffert and Herold, 1995], hereafter RH) because the later work directly used the general relativistic Euler equation to derive the gravity-pressure balance equation, whereas in the first work the general relativistic version of the gravity-pressure balance equation was not directly derived. NT took the Newtonian gravity-pressure balance equation and replaced the vertical component of gravity pressure balance with $R_{0z0}^z z$.

In recent years, Abramowicz, Lanza and Percival ([Abramowicz et al., 1997], hereafter ALP) have provided a novel expression for disc thickness. In these calculations, ALP also derived the same gravity-pressure balance equation from the general relativistic equation. But while simplifying the equation they replaced the four velocity component in such a way that no singularity in the disc height occurs at horizon. The main modification apart from this careful choice of four velocity is that ALP used only one component of the relativistic Euler equation whereas RH did not assume trivial forms of four velocities and solved two equations simultaneously for two components of the relativistic Euler equation.

In our present work, we will formulate and solve the general relativistic Euler and the continuity equations to observe how the aforementioned three different prescriptions for the flow thickness influence the properties of the stationary integral flow solutions having more than one sonic transitions and incorporating standing shock. Accretion flow governed by the polytropic as well as the isothermal equation of state will be studied.

We shall learn that for shock formation in isothermal flow, considerable amount of energy may be released at the shock, which may enhance the brightness of the otherwise advection-dominated radiatively inefficient disc near the shock and such mechanism may explain the details of the flares emanating out of the black hole accretion disc as observed in various wavebands of the electromagnetic spectrum ([Karssen et al., 2017], [Mossoux and Grosso, 2017], [Roberts et al., 2017], [Mossoux et al., 2020]).

Our work, thus, sheds light on how a proposed flow thickness may contribute to understand the variation of the disc luminosity during the generation of flares. The present work may also be useful in the context of analogue gravity phenomenon. It has been observed that a curved acoustic metric may be embedded within the accreting matter and such space-time may be generated through the perturbation of accretion flow ([Ananda et al., 2015], [Bollimpalli et al., 2017], [Shaikh et al., 2017], [Shaikh and Das, 2018], [Shaikh, 2018], [Datta et al., 2018], [Shaikh et al., 2019], [Datta and Das, 2019]). The present work will also lead

to the understanding of how the flow thickness of axially symmetric accretion in the Kerr metric may influence the properties of the analogue surface gravity of the corresponding sonic space-time.

Overall, the technical procedures followed to accomplish our goal are summarized below –

For three expressions of the flow thickness as classified in previous paragraphs, we shall formulate and solve the general relativistic Euler equation and the equation of continuity for ideal relativistic fluid, by assuming that the viscous transport of angular momentum may not play significant role for low angular momentum accretion flow. We shall then solve such equations for steady state flows and obtain stationary integral flow solutions which may make transitions from subsonic to supersonic state twice. We then introduce and discuss the mathematical conditions governing the formation of general relativistic standing shock, and solve such equations to obtain the shock location as a function of black hole spin angular momentum, i.e. the Kerr parameter. The properties of hotter, denser and shock-compressed post-shock flow is then studied as the function of the Kerr parameter and the influence of the expression to the flow thickness on such properties is then realized.

2 Model

2.1 Physical space-time

We represent the physical space-time of an uncharged, rotating black hole along its equatorial plane using the Kerr metric written in cylindrical Boyer-Lindquist coordinates ([Boyer and Lindquist, 1967]). The choice of co-ordinates is in accordance with cylindrical symmetry of the discs. Also for simplicity, we are interested in projection of the flow variables on the equatorial plane, obtained using vertical averaging technique as explained in subsequent sections. The line element for such a metric is given by,

$$ds^2 = -\frac{r^2\Delta}{A}dt^2 + \frac{A}{r^2}(d\phi - \omega dt)^2 + \frac{r^2}{\Delta}dr^2 + dz^2, \quad (1)$$

where

$$\Delta = r^2 - 2r + a^2, \quad A = r^2 + r^2a^2 + 2ra^2, \quad \omega = \frac{2ar}{A}. \quad (2)$$

ω represents the rate of frame dragging by the black hole, a being the Kerr parameter which in turn is related to the spin angular momentum J of the black hole through the relation $a = J/M_{BH}c$, where $-1 < a < 1$, M_{BH} is the mass of the respective black hole and c is the velocity of light in vacuum. Calculations have been carried out using natural units, i.e. $G = c = 1$ where G is the universal gravitational constant. All masses are measured in units of M_{BH} which has been set to 1 for algebraic convenience and can be easily substituted back using simple dimensional analysis. Distances are measured in units of GM_{BH}/c^2 , times are measured in units of GM_{BH}/c^3 and all velocities are scaled in units of c . For a Kerr black hole, the horizon is located at the outer boundary of $g^{rr} = \Delta/r^2 = 0$, which is defined as r_+

and the expression of which is given by,

$$r_+ = 1 + \sqrt{1 - a^2}. \quad (3)$$

2.2 Choice of disc height

We consider accretion disc around Kerr black hole in hydrostatic equilibrium along vertical direction, i.e, the gravitational force component is balanced by the pressure of the fluid constituting the disc. The earliest general relativistic formulation of this gravity-pressure balance and thus a vertically averaged height prescription proposed by NT ([Novikov and Thorne, 1973]) is given by,

$$H_{NT}(r) = \left(\frac{p}{\rho}\right)^{\frac{1}{2}} \frac{r^3 + a^2 r + 2a^2}{r^{\frac{3}{2}} + a} \sqrt{\frac{r^6 - 3r^5 + 2ar^{\frac{9}{2}}}{(r^2 - 2r + a^2)(r^4 + 4a^2 r^2 - 4a^2 r + 3a^4)}}, \quad (4)$$

where p and ρ are pressure and rest-mass energy density of the fluid respectively. It is to be noted that accretion flow described by the above disc thickness can not be extended upto r_+ . The flow will be truncated at a *truncation radius* r_T , which is given by solution of the equation,

$$(r_T)^{\frac{1}{2}} (r_T - 3) = 2a, \quad (5)$$

and which is greater than r_+ . In reality of course the flow will exist upto r_+ , but stationary integral flow solutions can not be formulated in the vicinity of r_+ for NT-type of discs.

The next prescription found in literature dealing with gravity-pressure balance and proposing a height recipe in the Kerr metric was by RH ([Riffert and Herold, 1995]). They modified the gravity-pressure balance condition of the treatment done in NT. Their proposed disc height is given by,

$$H_{RH}(r) = \left(\frac{p}{\rho}\right)^{\frac{1}{2}} \sqrt{\frac{r^5 - 3r^4 + 2ar^{\frac{7}{2}}}{r^2 - 4ar^{\frac{1}{2}} + 3ar^2}} \quad (6)$$

Here also, the flow can only be extended inwardly upto r_T , which has the same value for NT and RH discs around the same black hole as given by eqn.(5).

Thus we see that both the disc heights can be expressed in the form by $H(r) = \left(\frac{p}{\rho}\right)^{\frac{1}{2}} f(r, a)$. The difference between these two models of disc thickness in vertical equilibrium is reflected by the difference in functional form of two different $f(r, a)$. The essential difference arises because whereas NT balanced the vertical component of pressure with a particular Riemann tensor R_{0z0}^z , which was equivalent to the vertical component of gravitational acceleration, RH derived the gravity-pressure balance equation by simultaneously solving two orthogonal projection components of the general relativistic Euler equation. We will observe that the Mach number evaluated at the critical points corresponding to the flow described by the thickness function proposed by NT will be identical with that of the flow described by the thickness functions proposed by RH. This is evident because the dynamical equation will

have the same form in terms of $f(r, a)$, because the height recipe also has a similar form.

ALP ([Abramowicz et al., 1997]) introduced an expression for the disc thickness, given by

$$H_{ALP}(r) = \left(\frac{p}{\rho}\right)^{\frac{1}{2}} \sqrt{\frac{2r^4}{v_\phi^2 - a^2(v_t - 1)}}. \quad (7)$$

Here, v^μ denotes the four-velocity of the fluid in an azimuthally-boosted frame that co-rotates with the flow. v_ϕ and v_t are the azimuthal and temporal components of the covariant 4-velocity respectively which are related by $\lambda = -v_\phi/v_t$, where λ is the specific angular momentum of the flow and v_t is given by,

$$v_t = \sqrt{\frac{\Delta}{B(1 - u^2)}}, \quad (8)$$

where $B = g_{\phi\phi} + 2\lambda g_{t\phi} - \lambda^2 g_{tt}$ and u denotes advective velocity which is the three-component velocity in the co-rotating frame.¹ As mentioned earlier, no singularities in ALP-type disc heights occur at the horizon. Thus, ALP discs do not have any truncation constraints and the steady state accretion solutions can be obtained upto r_+ .

3 Polytropic accretion

3.1 Fluid equations

3.1.1 Fluid specification and sound speed

As specified earlier, we consider a low angular momentum accretion disc. The low angular momentum prevents the inward part of the disc to transfer momentum to the outside region. Thus we consider a perfect fluid as the constituent of the accretion disc. The energy momentum tensor for a perfect fluid is given by

$$T^{\mu\nu} = (p + \epsilon)v^\mu v^\nu + pg^{\mu\nu}, \quad (9)$$

where ϵ is the total energy density of the fluid given by $\epsilon = \rho + \epsilon_{\text{thermal}}$, where $\epsilon_{\text{thermal}}$ is the internal thermal energy density of the fluid.

The equation of state for adiabatic flow is given by $p = k\rho^\gamma$ where γ is the polytropic index and k is a constant. Whereas for isothermal case $p \propto \rho$. The sound speed for adiabatic flow (isentropic flow) is given by

$$c_s^2 = \left. \frac{\partial p}{\partial \epsilon} \right|_{\text{entropy}} = \frac{\rho}{h} \frac{\partial h}{\partial \rho}, \quad (10)$$

¹we refer [Gammie and Popham, 1998] for the detailed description of expressions of various velocities in different frames for rotating accretion flow in the Kerr metric

where h is the enthalpy given by

$$h = \frac{p + \varepsilon}{\rho}. \quad (11)$$

3.1.2 Conservation of specific energy

The energy-momentum conservation equation can be written as

$$D_\mu T^{\mu\nu} = 0, \quad (12)$$

where D_μ is the covariant derivative operator with respect to μ . Eqn.(12), in turn, can be written using the definition of sound speed as

$$(p + \varepsilon)v^\mu D_\mu v^\nu + (v^\mu v^\nu + g^{\mu\nu})\partial_\mu p = 0. \quad (13)$$

Now the thermodynamic equation of motion is given by

$$T\partial_\mu s = \partial_\mu h - \frac{\partial_\mu p}{\rho} \quad (14)$$

where s is the specific entropy. In case of polytropic accretion, right hand side of Eqn. (14) is zero and Eq. (13) can be rewritten using normalization of four velocity, which yields

$$u^\nu [D_\nu(hu_\mu) - D_\mu(hu_\nu)] = 0 \quad (15)$$

Using time component of the equation and the fact that the flow is stationary, the conserved quantity from energy-momentum conservation equation in case of polytropic accretion turns out to be

$$\mathcal{E} = hv_t = \text{constant}. \quad (16)$$

Substituting for v_t from eqn.(8) and h from eqn.(11) we obtain,

$$\mathcal{E} = \frac{\gamma - 1}{\gamma - 1 - c_s^2} \sqrt{\frac{\Delta}{B(1 - u^2)}} \quad (17)$$

Taking logarithmic derivative of both sides of equation (17) gives the gradient of sound speed as

$$\frac{dc_s}{dr} = -\frac{\gamma - 1 - c_s^2}{2c_s} \left[\frac{u}{1 - u^2} \frac{du}{dr} + \frac{1}{2} \left(\frac{\Delta'}{\Delta} - \frac{B'}{B} \right) \right] \quad (18)$$

3.1.3 Conservation of mass

The mass conservation equation is given by

$$D_\mu(\rho v^\mu) = 0. \quad (19)$$

A vertical averaging is done for convenience by integrating the flow equations over the z co-ordinate and the resultant equation is described by the flow variables defined on the equatorial plane ($z = 0$). Furthermore, integration is done over ϕ which gives a factor of

2π due to the axial symmetry of the flow. We apply such vertical averaging as prescribed in ([Novikov and Thorne, 1973], [Matsumoto et al., 1984], [Gammie and Popham, 1998]) to the continuity equation given by Eq. (19). The vertically averaged z -component of the 4-velocity becomes $v^z \sim 0$. Thus for the stationary (t -independent) and axially symmetric (ϕ -independent) flow, the continuity equation turns out to be

$$\frac{\partial}{\partial r}(4\pi H_\theta \sqrt{-g} \rho v^r) = 0 \quad (20)$$

H_θ arises due to the vertical averaging and is the local angular scale of flow. One can relate the actual local flow thickness $H(r)$ to the angular scale of the flow H_θ as $H_\theta = H(r)/r$, where r is the radial distance along the equatorial plane from the centre of the disc. g is the value of the determinant of the metric $g_{\mu\nu}$ on the equatorial plane, $g = \det(g_{\mu\nu})|_{z=0} = -r^4$. The equation (20) gives the mass accretion rate \dot{M} as

$$\dot{M} = 4\pi \sqrt{-g} H_\theta \rho v^r = 4\pi H(r) r \rho v^r. \quad (21)$$

The r component of the four velocity, v^r is related to u by the transformation law as

$$v^r = \frac{u}{\sqrt{g_{rr}(1-u^2)}} = \frac{\sqrt{\Delta} u}{r\sqrt{1-u^2}} \quad (22)$$

using $g_{rr} = r^2/\Delta$, \dot{M} can be written as

$$\dot{M} = 4\pi H(r) \Delta^{1/2} \rho \frac{u}{\sqrt{1-u^2}} = \text{constant} \quad (23)$$

For adiabatic flow, a new quantity $\dot{\Xi}$ is obtained from \dot{M} by multiplying it with $(\gamma k)^{\frac{1}{\gamma-1}}$. $\dot{\Xi}$ is a measure of entropy accretion rate and typically called as the entropy accretion rate. The concept of the entropy accretion rate is widely used in accretion astrophysics. The entropy accretion rate was first defined in the literature by [Abramowicz and Zurek, 1981] and [Blaes, 1987]. Expressing ρ in terms of γ , k and c_s gives

$$\dot{\Xi} = \left(\frac{(\gamma-1)c_s^2}{\gamma-1-c_s^2} \right)^{\frac{1}{\gamma-1}} 4\pi H(r) \Delta^{1/2} \frac{u}{\sqrt{1-u^2}} = \text{constant} \quad (24)$$

To express the entropy density in terms of u , c_s and r only, the expression of height must be written in terms of u and c_s also. For this we first note that, for adiabatic equation of state, p/ρ can be written as

$$\frac{p}{\rho} = \left(\frac{1}{\gamma} \right) \left(\frac{(\gamma-1)c_s^2}{\gamma-1-c_s^2} \right) \quad (25)$$

This factor is common to all the height recipes. Now, for convenience, we distinguish the height recipes in two classes, one consisting of NT and RH. The other has ALP model as its member. The reason behind this classification is that whereas the models in the first class can be written in generally as $H(r) = (\frac{p}{\rho})^{\frac{1}{2}} f(r, a)$, the model in the other class can not be written as such. Thus we proceed separately for this two classes and derive the desired velocity gradients.

NT and RH-type of discs For these two models, we can write $H(r)$ from Eq. (4) and Eq.(6) as

$$H(r) = \left(\frac{1}{\gamma}\right)^{1/2} \left(\frac{(\gamma-1)c_s^2}{\gamma-1-c_s^2}\right)^{1/2} f(r, a) \quad (26)$$

where for NT

$$f_{NT}(r, a) = \frac{r^3 + a^2r + 2a^2}{r^{\frac{3}{2}} + a} \sqrt{\frac{r^6 - 3r^5 + 2ar^{\frac{9}{2}}}{(r^2 - 2r + a^2)(r^4 + 4a^2r^2 - 4a^2r + 3a^4)}}. \quad (27)$$

and for RH

$$f_{RH}(r) = \sqrt{\frac{r^5 - 3r^4 + 2ar^{\frac{7}{2}}}{r^2 - 4ar^{\frac{1}{2}} + 3ar^2}} \quad (28)$$

Using the expression of $H(r)$ for both these models, $\dot{\Xi}$ can be written as

$$\dot{\Xi} = \sqrt{\frac{1}{\gamma}} \left(\frac{(\gamma-1)c_s^2}{\gamma-1-c_s^2}\right)^{\frac{\gamma+1}{2(\gamma-1)}} 4\pi\Delta^{1/2} \frac{u}{\sqrt{1-u^2}} f(r, a) \quad (29)$$

Taking logarithmic derivative of both sides of the above equation and substituting dc_s/dr using Eq. (18) gives

$$\frac{du}{dr} = \frac{u(1-u^2) \left[\frac{2}{\gamma+1} c_s^2 \left(\frac{\Delta'}{2\Delta} + \frac{f'}{f} \right) + \frac{1}{2} \left(\frac{B'}{B} - \frac{\Delta'}{\Delta} \right) \right]}{u^2 - \frac{c_s^2}{(\frac{\gamma+1}{2})}} = \frac{N}{D}. \quad (30)$$

ALP-type of discs From eqn. (7) and using the relation $\lambda = -\frac{v_\phi}{v_t}$, we have

$$H(r) = H_{ALP}(r) = \left(\frac{1}{\gamma}\right)^{1/2} \left(\frac{(\gamma-1)c_{s0}^2}{\gamma-1-c_{s0}^2}\right)^{1/2} \sqrt{\frac{2r^4}{\lambda^2 v_t^2 - a^2(v_t - 1)}}, \quad (31)$$

Thus using this expression of $H(r)$, $\dot{\Xi}$ can be expressed as

$$\dot{\Xi} = \sqrt{\frac{1}{\gamma}} \left(\frac{(\gamma-1)c_s^2}{\gamma-1-c_s^2}\right)^{\frac{\gamma+1}{2(\gamma-1)}} 4\pi\Delta^{1/2} \frac{u}{\sqrt{1-u^2}} \sqrt{\frac{2r^4}{\lambda^2 v_t^2 - a^2(v_t - 1)}} \quad (32)$$

Taking logarithmic derivative of the entropy accretion rate and using Eq. (18) to replace $\frac{dc_s}{dr}$ we yield

$$\frac{du}{dr} = \frac{\frac{2c_s^2}{\gamma+1} \left(-\frac{Pv_t(2\lambda^2v_t-a^2)}{4F} + \frac{\Delta'}{2\Delta} + \frac{2}{r} \right) - \frac{P}{2}}{\frac{u}{1-u^2} - \frac{2c_s^2}{\gamma+1} \frac{1}{(1-u^2)u} \left(1 - \frac{u^2v_t(2\lambda^2v_t-a^2)}{2F} \right)} = \frac{N}{D} \quad (33)$$

where $P = \frac{\Delta'}{\Delta} - \frac{B'}{B}$ and $F = \lambda^2 v_t^2 - a^2(v_t - 1)$.

3.2 Critical point conditions

In this section, we will present the scheme and calculations for finding stationary transonic flow solutions for all the three height recipes. We present NT and RH discs in the first class and ALP discs in the second class for reasons stated earlier.

3.2.1 NT and RH-type of discs

Borrowing a standard recipe from the theory of dynamical systems ([Jordan and Smith, 1999], [Strogatz, 2001],[Hilborn, 2001]), we set the numerator and denominator of du/dr to zero separately in order to obtain the necessary conditions to be satisfied at the critical points of the system. Setting $D = 0$ we get,

$$u^2|_c = c_s^2|_c / \left(\frac{\gamma + 1}{2}\right) \quad (34)$$

where the suffix c denotes its value evaluated at the critical point. By setting $N = 0$, we yield

$$c_s^2|_c = \left(\frac{\gamma + 1}{4}\right) \frac{\frac{B'}{B} - \frac{\Delta'}{\Delta}}{\left(\frac{\Delta'}{2\Delta} + \frac{f'}{f}\right)}. \quad (35)$$

In order to solve for the critical points, the critical point condition (34) is used in (17), which gives

$$\mathcal{E} = \frac{\gamma - 1}{\gamma - 1 - (c_s^2)_c} \sqrt{\frac{(\gamma + 1)\Delta_c}{B_c(\gamma + 1 - 2(c_s^2)_c)}} \quad (36)$$

where $(c_s^2)_c$ is a function of r and Kerr parameter a obtained from (35). The solutions of this equation for a given set of system parameters $[\mathcal{E}, \lambda, \gamma, a]$, provide the critical points. The number of such critical points may be more than one depending on the parameter values.

Now the value of $\frac{du}{dr}$ at critical point is obtained by using L'Hospital's rule in (30) as both the numerator and denominator tends to zero at critical point. Then one obtains a quadratic equation of the form

$$\alpha_1 \left(\frac{du}{dr}\right)^2 - \alpha_2 \left(\frac{du}{dr}\right) - \alpha_3 = 0, \quad (37)$$

where

$$\alpha_1 = 2(u)_c \left[1 - \frac{((c_s^2)_c - \gamma - 1)}{(\gamma + 1)(1 - (u^2)_c)}\right], \quad (38)$$

$$\begin{aligned} \alpha_2 = & \frac{((c_s^2)_c - \gamma - 1)}{(\gamma + 1)} \left(\frac{\Delta'}{\Delta} - \frac{B'}{B} + \left(\frac{\Delta'}{\Delta} + \frac{2f'_{\text{NT}}}{f_{\text{NT}}}\right) (u^2)_c\right) \\ & + \left[\frac{2}{\gamma + 1} (c_s^2)_c \left(\frac{\Delta'}{2\Delta} + \frac{f'_{\text{NT}}}{f_{\text{NT}}}\right) + \frac{1}{2} \left(\frac{B'}{B} - \frac{\Delta'}{\Delta}\right)\right] (1 - 3(u^2)_c), \quad (39) \end{aligned}$$

$$\alpha_3 = (u)_c (1 - (u^2)_c) \left[\frac{1}{2} \frac{\alpha'^2}{\alpha} - \frac{\alpha''}{2\alpha} + \frac{2(c_s^2)_c}{\gamma + 1} \left(\frac{\Delta''}{2\Delta} + \frac{f''}{f} - \frac{1}{2} \frac{\Delta'^2}{\Delta} - \frac{f'^2}{f} \right) + \frac{((c_s^2)_c - \gamma - 1)}{(\gamma + 1)} \left(\frac{\Delta'}{2\Delta} + \frac{f'}{f} \right) \left(\frac{\Delta'}{\Delta} - \frac{B'}{B} \right) \right]. \quad (40)$$

The two roots of above quadratic equation (37) signify two different slopes of two different integral solutions passing through each critical point, while such slopes are measured at the respective critical points only.

Once we are equipped with the critical points and the critical gradients, the phase-space portrait (i.e., u vs. r diagram) can be plotted by numerically integrating the expression of du/dr (eqn. (30)) for a particular set of $[\mathcal{E}, \lambda, \gamma, a]$ as will be illustrated in the subsequent sections. Here we substitute the value of c_s^2 from eqn. (24) as a function of parameter \mathcal{E} , r and u . While addressing transonicity-related aspects of the flow, it is usually convenient to use the Mach number ($M = u/c_s$) instead of the advective flow velocity u .

3.2.2 ALP-type of discs

By setting $N = 0$ and $D = 0$, the critical conditions turn out to be

$$u^2|_{r_c} = \frac{P}{\frac{\Delta'}{\Delta} + \frac{4}{r}}|_{r_c}, \quad (41)$$

and

$$c_s^2|_{r_c} = \frac{(\gamma + 1)(2Fu^2)}{2(2F - u^2v_t(2\lambda^2v_t - a^2))}|_{r_c} \quad (42)$$

To find the critical point we use the critical condition (42) in eqn. (17) and then solve the equation.

As observed from eqns. (34), (41) and (42), the value of the Mach number at the critical point differs from unity for all three disc models considered in the present work. Hence the critical points do not coincide with the sonic points – by definition the sonic point is the location where the Mach number becomes unity. The value of the Mach number at critical points are found out to be less than unity for all three type of disc thicknesses. For NT and RH kind of flow, the Mach number at the critical point is a constant $\left(\sqrt{\frac{2}{\gamma+1}}\right)$ for a fixed value of γ . The departure of the value of the Mach number from unity has the same numerical value for all three critical points and hence three critical points lie on the same horizontal line parallel to the abscissa. For isothermal accretion, the value of the polytropic index γ will be one, and hence for isothermal flow, the critical and the sonic points will be the same for NT as well as for RH-type of flow.

For ALP-type of disc, however, the amount of departure of Mach number (measured at the critical point) from unity is not constant. It rather depends on the value of the critical point

itself. Thus for ALP type of disc, three different critical points for multi-critical accretion will assume three different values of the Mach number, and three critical points will not lie of the same horizontal line for such disc model. For ALP-type of disc, even for the isothermal flow, the Mach number does not become unity at the critical point.

Given a set of values of $[\mathcal{E}, \lambda, \gamma, a]$, one obtains the location of the critical point through the critical point analysis and it is not required to integrate the fluid equations (the Euler equation or the equation of continuity). Among three critical points, the middle one is of centre-type and hence no physical accretion solution can pass through it. Accretion solution can pass through the inner and outer critical points only. Hence, one can have the sonic points corresponding to these two critical points since both the inner and the outermost critical points are of saddle-type. One thus computes the location of the critical point algebraically as discussed in sections 3.2.1 and 3.2.2, and then integrates the flow equations, starting from the critical point, up to the value of r where the value of the Mach number becomes unity. That point is defined as the sonic point. We thus need to construct the integral accretion solution to find out the location of the sonic points corresponding to the inner-type and the outer-type critical points.

By following the same procedure as used to derive the slopes of trajectories through critical points, we find

$$\frac{du}{dr}\Big|_{r_c} = -\frac{\beta_{VE}}{2\alpha_{VE}} \pm \frac{1}{2\alpha_{VE}} \sqrt{\beta_{VE}^2 - 4\alpha_{VE}\Gamma_{VE}} \quad (43)$$

where the co-efficients α_{VE} , β_{VE} and Γ_{VE} are given by,

$$\begin{aligned} \alpha_{VE} &= \frac{1+u^2}{(1-u^2)^2} - \frac{2nD_2D_6}{2n+1}, \quad \beta_{VE} = \frac{2nD_2D_7}{2n+1} + \tau_4, \quad \Gamma_{VE} = -\tau_3, \\ n &= \frac{1}{\gamma-1}, \quad D_2 = \frac{c_s^2}{u(1-u^2)} (1 - D_3), \quad D_6 = \frac{3u^2-1}{u(1-u^2)} - \frac{D_5}{1-D_3} - \frac{(1-nc_s^2)u}{nc_s^2(1-u^2)}, \\ D_7 &= \frac{1-nc_s^2}{nc_s^2} \frac{P1}{2} + \frac{D_3D_4v_tP1}{2(1-D_3)}, \quad \tau_3 = \frac{2n}{2n+1} \left(c_s^2\tau_2 - \frac{v_tP1v_1}{2nv_t} (1 - nc_s^2) - c_s^2v_5v_t \frac{P1}{2} \right) - \frac{P1'}{2}, \\ \tau_4 &= \frac{2n}{2n+1} \frac{v_tu}{1-u^2} \left(\frac{v_1}{nv_t} (1 - nc_s^2) + c_s^2v_5 \right), \quad v_1 = \frac{\Delta'}{2\Delta} + \frac{2}{r} - (2\lambda^2v_t - a^2) v_t \frac{P1}{4F}, \\ D_3 &= \frac{u^2v_t(2\lambda^2v_t - a^2)}{2F}, \quad D_4 = \frac{1}{v_t} + \frac{2\lambda^2}{2\lambda^2v_t - a^2} - \frac{2\lambda^2v_t - a^2}{F}, \quad D_5 = D_3 \left(\frac{2}{u} + \frac{D_4v_tu}{1-u^2} \right), \quad \tau_2 = \tau_1 - \frac{v_t(2\lambda^2v_t - a^2)}{4F} P1', \\ v_5 &= (2\lambda^2v_t - a^2) \frac{P1}{4F} v_4, \\ \tau_1 &= \frac{1}{2} \left(\frac{\Delta''}{\Delta} - \frac{(\Delta')^2}{\Delta^2} \right) - \frac{2}{r^2}, \quad v_4 = \frac{v_3}{(2\lambda^2v_t - a^2)F}, \quad v_3 = (4\lambda^2v_t - a^2) F - (2\lambda^2v_t - a^2)^2 v_t. \end{aligned}$$

3.3 Parameter space

Having presented the complete scheme of drawing the phase-space portrait numerically, we focus our attention on the parameter space of the system. \mathcal{E} is scaled by rest-mass energy and includes both rest-mass energy and thermal energy components. Setting $\mathcal{E} = 1$ corresponds to an initial state where no thermal energy is present. Furthermore, setting $\mathcal{E} < 1$ corresponds to initial conditions with negative energy. In this case, a dissipative mechanism is needed to extract energy from the flow so that a flow solution is obtained with positive energy. For our system of inviscid flow, this is not possible and thus we must consider flows with $\mathcal{E} > 1$. All values of \mathcal{E} greater than 2, although possible, correspond to extremely high initial thermal energy. Since this is not a common feature of accreting black hole systems,

it is usual to restrict the system within the parameter range $1 < \mathcal{E} < 2$.

$\lambda = 0$ implies a spherically symmetric flow, where $\lambda > 4$ (in $G = M_{BH} = c = 1$ scaling) implies that the flow is not anymore in the Keplerian regime. In this region, multi-critical solutions do not generally occur. Thus we restrict ourselves to the parameter range of $0 < \lambda < 4$.

In isothermal fluids, polytropic index $\gamma = 1$. $\gamma > 1$ corresponds to extremely dense fluids where comparatively large magnetic fields with direction dependence, i.e, anisotropic pressure are present. As we are not considering general relativistic magneto-hydrodynamics, we should constrain ourselves in the domain $1 < \gamma < 2$. Moreover, throughout literature, the realistic limits to polytropic index for accretion astrophysics is $\gamma = \frac{4}{3}$ for ultra-relativistic flows and $\gamma = \frac{5}{3}$ for non-relativistic flows. Thus we will limit ourselves in the parametric range between $\frac{4}{3} < \gamma < \frac{5}{3}$.

Here we mention pro-grade flows, i.e. where the flow co-rotates with black hole and retro-grade flows, i.e. where the flow counter-rotates with black hole. We consider both these flows and in order to distinguish between the two, we allow positive and negative values of a , whereas only positive values of λ are allowed. Thus the range of a is $-1 < a < 1$. An upper limit of 0.998 of a has been set in some literature where interaction with accretor and the accreting material has been considered ([Thorne, 1974]). In his work, Thorne considered the interaction of the accretion flow with the hole in such a way, that the accretion flow can alter the mass and spin of the hole, which, however, we do not consider in our present work. Thus, the present system of polytropic fluid accretion is studied within the parameter range $[1 < \mathcal{E} < 2, 0 < \lambda < 4, \frac{4}{3} < \gamma < \frac{5}{3}, -1 < a < 1]$.

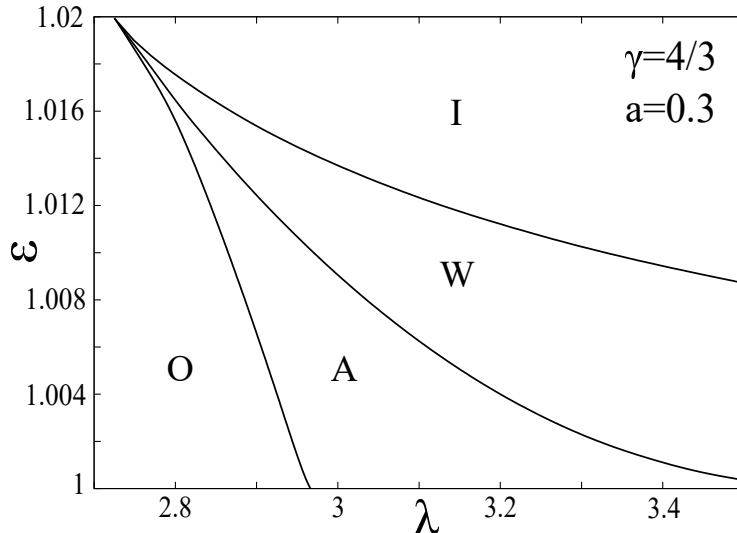


Figure 1: \mathcal{E} vs. λ plot for polytropic NT disc with $a = 0.3$ and $\gamma = 4/3$

Fig. (1) depicts the characteristic parameter space diagram for a polytropic NT disc. The NT disc has been selected for the purpose of demonstration because it is the oldest prescription of hydrostatic equilibrium discs available in literature. All other prescriptions display the same

general properties in this regard. For a fixed set of $[\gamma, a]$, possible multi-critical solutions form a wedge-shaped projection on the $\mathcal{E} - \lambda$ plane. The multi-critical solutions constitute a set of three critical points, viz. r_c^{in} , r_c^{mid} and r_c^{out} , such that $r_c^{in} < r_c^{mid} < r_c^{out}$. The region A represents the ‘accretion solutions’ for which the entropy accretion rate, $\dot{\Xi}(r_c^{in}) > \dot{\Xi}(r_c^{in})$. The region W consists of those solutions for which $\dot{\Xi}(r_c^{in}) > \dot{\Xi}(r_c^{in})$. Such solutions are known as ‘wind solutions’. The curve dividing regions A and W covers those critical points through which *heteroclinic orbits* are formed in phase-space. Slight perturbations in the flow due to turbulence or other physical factors can push such solutions into either accretion or wind regime. Regions outside the wedge (O and I) contain mono-critical solutions. Inside region O , the critical point is of outer-type, which means it forms far away from the horizon, whereas inside region I , the critical points are formed nearer to the horizon and are known as inner-type. Both regions O and I contain single critical points (corresponding to mono-transonic accretion/wind) upto a certain limit of flow parameters beyond which critical solutions cease to exist. However, since we are interested only in the A region, a detailed discussion regarding the relation between system parameters and the existence or non-existence of critical points lies beyond the scope of the present article.

3.4 General relativistic polytropic shock conditions

Since, we have assumed a non-dissipative, inviscid flow, the specific energy and mass accretion rate are conserved. Thus, shocks formed in such flows must also preserve the conserved quantities. We consider the shock surface to be infinitesimally thin such that there are no temperature gradients within shock leading to any unwanted dissipation. Hence the discontinuity must satisfy the general relativistic Rankine-Hugoniot conditions ([Eckart, 1940], [Taub, 1948], [Lichnerowicz, 1967], [Thorne, 1973], [Taub, 1978], [Hacyan, 1982], [Abraham et al., 2006]) given below.

$$\begin{aligned}
[[\rho v^\mu \eta_\mu]] &= [[\rho v^r]] = 0 \\
[[T_{t\mu} \eta^\mu]] &= [[(p + \varepsilon) v_t v^r]] = 0 \\
[[T_{\mu\nu} \eta^\mu \eta^\nu]] &= [[(p + \varepsilon)(v^r)^2 + p g^{rr}]] = 0
\end{aligned} \tag{44}$$

Where $\eta_\mu = \delta_\mu^r$ is orthonormal to the surface of shock formation. For any arbitrary flow variable f , $[[f]]$ is defined as $[[f]] = f_+ - f_-$, where f_+ and f_- are values of f just outside and inside the shock, respectively. The difference measures the discontinuity in the flow variable due to shock. The first condition is conservation of mass accretion rate and the other two conditions are energy-momentum conservation. These conditions must be satisfied at the location of shock formation. In order to find out the location of shock formation, a shock invariant quantity, which depends only on u, c_s and γ , is constructed using the conditions above. The first and second conditions are trivially satisfied owing to the constancy of the mass accretion rate and the specific energy. The first condition is basically $(\dot{M})_+ = (\dot{M})_-$ and third condition is $(T^{rr})_+ = (T^{rr})_-$. Thus a shock invariant quantity S_{sh} can be defined as

$$S_{sh} = T^{rr} / \dot{M} \tag{45}$$

which also satisfies $[[S_{\text{sh}}]] = 0$.

In order to calculate the shock invariant quantity we note that h corresponds to the enthalpy of the stationary solutions of the steady state flow, given by equation Eq. (11). $c_s = (1/h)dp/d\rho = (1/h)k\gamma\rho^{\gamma-1}$, which gives ρ (and hence also p and ϵ) in terms of k, γ and c_s . Thus,

$$\begin{aligned}\rho &= k^{-\frac{1}{\gamma-1}} \left[\frac{(\gamma-1)c_s^2}{\gamma(\gamma-1-c_s^2)} \right]^{\frac{1}{\gamma-1}} \\ p &= k^{-\frac{1}{\gamma-1}} \left[\frac{(\gamma-1)c_s^2}{\gamma(\gamma-1-c_s^2)} \right]^{\frac{\gamma}{\gamma-1}} \\ \epsilon &= k^{-\frac{1}{\gamma-1}} \left[\frac{(\gamma-1)c_s^2}{\gamma(\gamma-1-c_s^2)} \right]^{\frac{1}{\gamma-1}} \left(1 + \frac{c_s^2}{\gamma(\gamma-1-c_s^2)} \right)\end{aligned}\quad (46)$$

Now $\dot{M} = \text{constant} \times rH(r)\rho v^r$ and $T^{rr} = (p + \epsilon)(v^r)^2 + pg^{rr}$, where $v^r = u/\sqrt{g_{rr}(1-u^2)}$.

NT & RH discs The shock-invariant quantity $S_{\text{sh}} = T^{rr}/\dot{M}$ becomes

$$S_{\text{sh}} = \frac{(u^2(\gamma - c_s^2) + c_s^2)}{uc_s\sqrt{(1-u^2)(\gamma-1-c_s^2)}} \quad (47)$$

where we have removed any over all factor of r as shock invariant quantity is to be evaluated at $r = r_{\text{sh}}$ for different branches of flow.

ALP discs In this case, the shock-invariant quantity turns out to be

$$S_{\text{sh}} = \frac{(u^2(\gamma - c_s^2) + c_s^2)\sqrt{\lambda^2 v_t^2 - a^2(v_t - 1)}}{uc_s\sqrt{(1-u^2)(\gamma-1-c_s^2)}} \quad (48)$$

where v_t is given in (8).

Fig.2(a) shows edge-on view of the polytropic NT disc for flow with a given value of $[\mathcal{E}, \lambda, \gamma, a]$ in the presence of shock. Since specific energy is conserved in polytropic accretion, the post-shock flow sees a discontinuous increase in temperature, density and pressure. Consequently, the disc gets ‘puffed-up’ at the shock location as is evident from the plot. A closer look at the central region of the disc (fig.2(b)) reveals that the disc gets terminated abruptly at a given radius, known as the ‘trauncation radius’ (r_T). The artefact, as discussed earlier, is due to the inherent mathematical limitation of the NT and RH class of discs regarding their closest approach of the event horizon. It limits the use of such discs for obtaining flow variables in close vicinity of the horizon (*quasi-terminal values*) that are essential for shadow-imaging of black holes ([Tarafdar et al., 2019]). Fig.(2(c)) depicts face-on view of one of the quadrants of the same disc on a logarithmic scale. The regions colored in cyan (lighter shade) and red (darker shade) represent regions of subsonic and supersonic flows

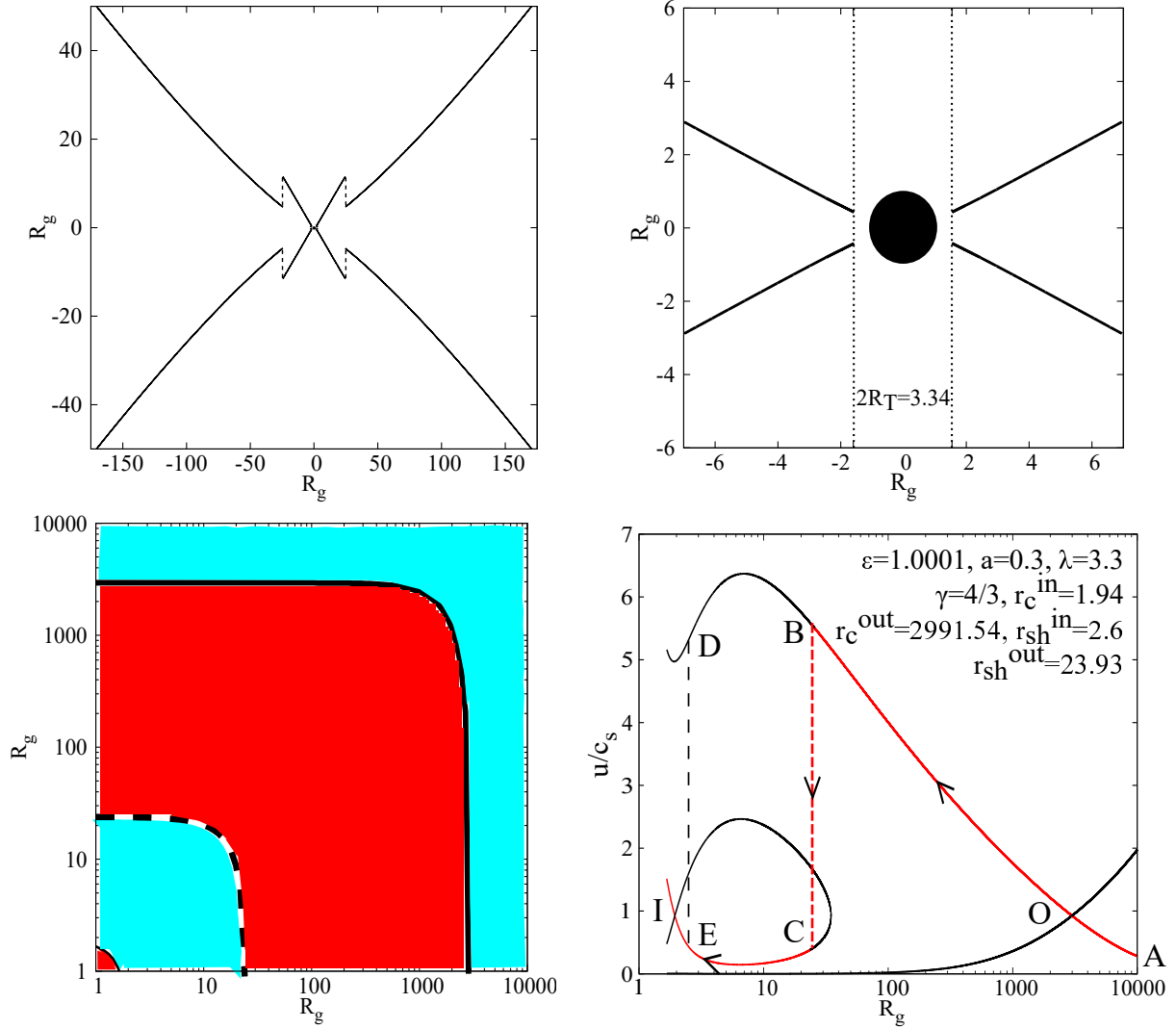


Figure 2: (a) Disc height vs. radial distance, (b) Central region in (a) is magnified, (c) Transonic boundaries - Cyan (lighter shade) region represents subsonic flow and red (darker shade) region represents supersonic flow, (d) Phase space trajectories - Mach number vs. radial distance

respectively. The solid boundary curves lie over points of continuous transonicity (transonic points corresponding to r_c^{out} and r_c^{in}), while the dashed boundary curve lies over the points of discontinuous transonicity, i.e. shock. The picture becomes clear in fig.(2(d)) where a complete phase-space profile (u/c_s vs. r) for the given combination of flow parameters has been presented. Trajectory of the physical flow (marked in red) in the presence of shock has been indicated with arrows. The flow starts subsonically through point A and proceeds to cross the first transonic point O (corresponding to the outer critical point r_c^{out}) beyond which it attains supersonic velocities till point B . Here the flow encounters shock, causing a discrete jump onto point C on the *homoclinic orbit*. The shock (dashed line BC) lies at the location r_{sh}^{out} , which can be calculated by looking for those values of r where S_{sh} on the upper and lower branches become equal in magnitude. Using this procedure, a second shock location (r_{sh}^{in} , shown with the black dashed line DE) is sometimes obtained such that $r_{sh}^{in} < r_{sh}^{out}$. But such inner second shocks have been found to be unstable in previous works (**references**). In the absence of shock, the flow would have continued supersonically along the upper branch through B , effectively resulting in mono-transonic accretion. However, transition onto C brings the flow down to subsonic regime, and subsequently it follows the trajectory of the lower branch through the second transonic point I (corresponding to the inner critical point r_c^{in}) and proceeds beyond to fall into the horizon.

In fig.(3), we plot the variation of the flow velocity u (fig.(3(a)), flow temperature T (fig.(3(b)), matter density ρ (fig.(3(c)) and the fluid pressure P (fig.(3(d)) as a function of the radial distance as measured from the horizon in terms of the Schwarzschild radius $R_g (= 2GM_{BH}/c^2)$. In fig.(3(a)-(d)), the variation is shown as a combination of two solid lines connected by a vertical dashed line. The solid line at the right of the dashed vertical line represents the variation along the flow solution passing through the outer sonic point (starting point of the solid line) and ending at the shock. The dashed vertical line corresponds to the discontinuous jump of the physical variable (u , T etc.) at the shock location. The solid line to the left of the dashed vertical line represents the variation along the integral flow solution starting from the shock location and ending at the corresponding truncation radius for NT/RF discs given by eqn. (5)). It is evident from the figure that the accretion flow slows down at the shock and gets compressed. Such relatively slow, shock-compressed post-shock flow becomes hotter and denser. The energy-preserving hotter flow adiabatically expands and hence the post-shock part of the disc gets puffed-up, as explained earlier.

As mentioned in introduction, our motivation is to compare various astrophysical properties of the shocked flow for three different disc thicknesses. We thus need to find out the region of the parameter space (parameters for which the shock forms) common to all such three different flow thicknesses.

In fig.(4(a)), we plot the $[\mathcal{E}, \lambda]$ regions for which the shock forms for the flow having thickness as prescribed by NT (blue dashed curve in the online version of this article), RH (green dotted curve in the online version) and ALP (red solid curve in the online version). It is to be mentioned that from now onwards, the line types (solid, dotted and dashed) and the line colors (red, green and blue) corresponding to the three different disc models (ALP, RH and NT respectively) will be used in the same order (as used in the present diagram) throughout

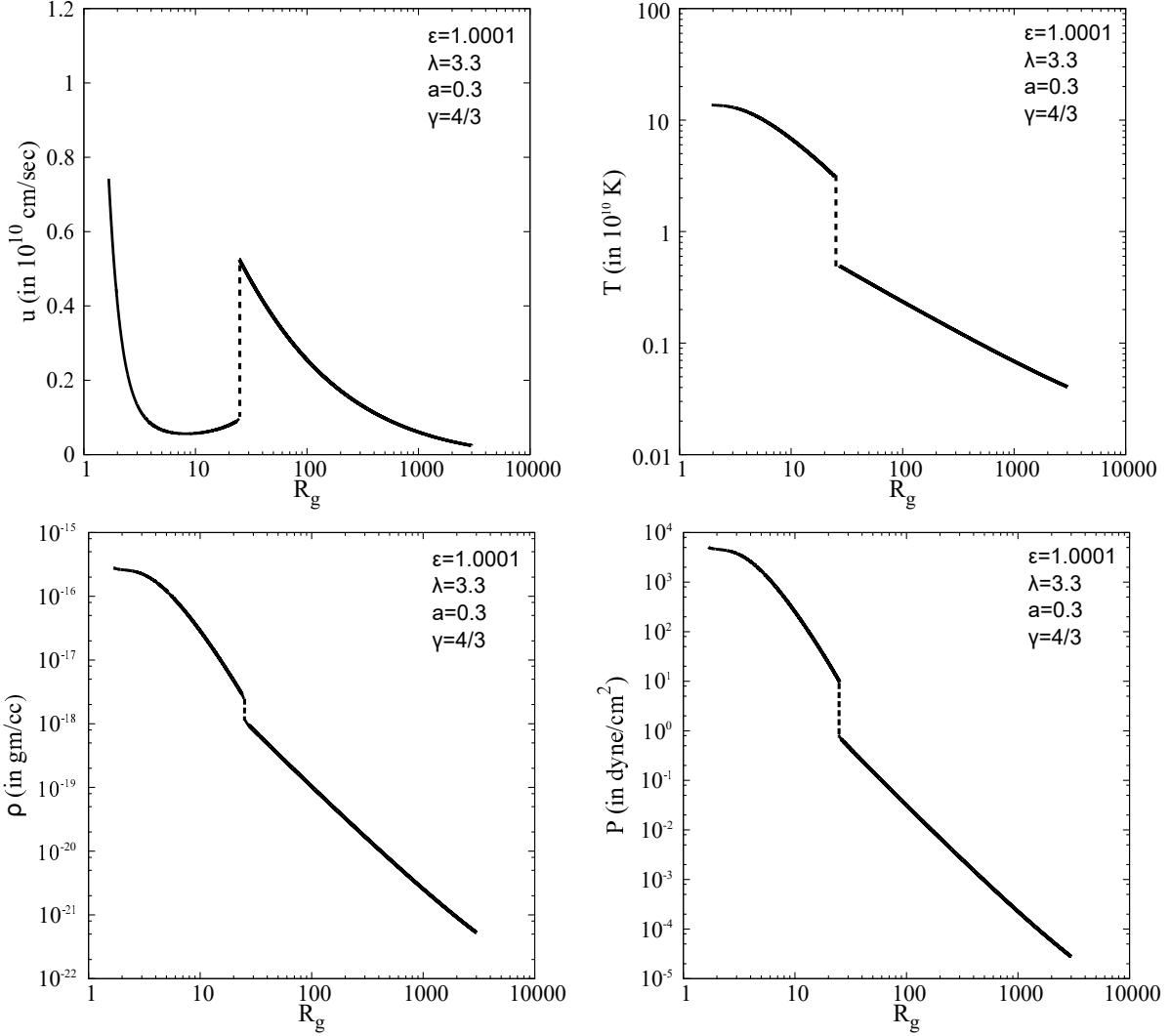


Figure 3: Generic flow profiles - (a) Advective velocity (u) vs. R_g , (b) Flow ion temperature (T) vs. R_g , (c) Rest mass density (ρ) vs. R_g (d) Pressure (P) vs. R_g . u is in units of 10^{10} cm/sec, T is in units of 10^{10} Kelvin, ρ is in units of gm/cc and P is in units of dyne/cm 2 .

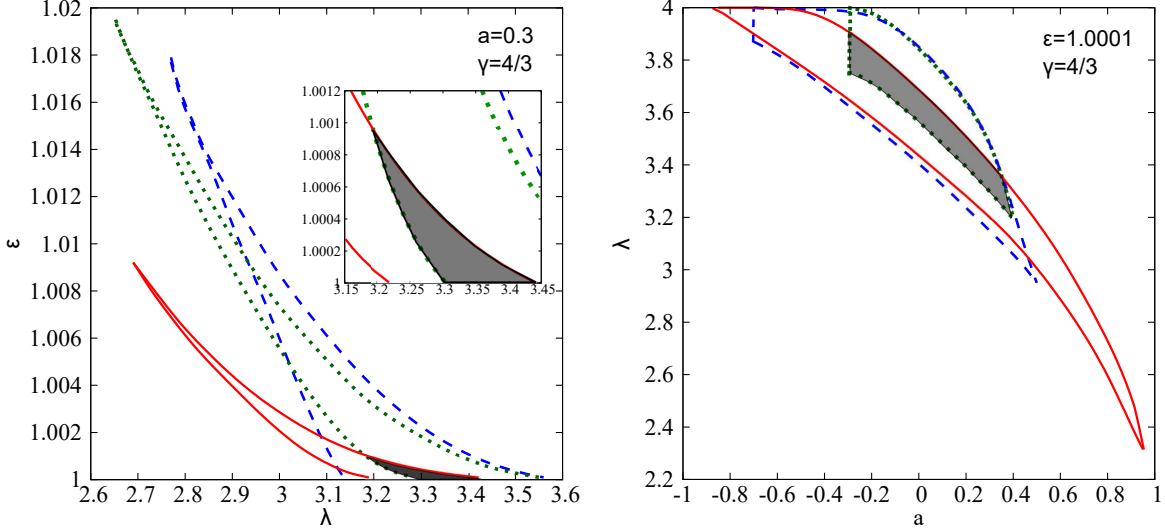


Figure 4: Parameter space overlap for shocked solution - (a) $\mathcal{E} - \lambda$ plot and (b) $\lambda - a$ plot. Insets and shaded areas depict the common regions of shock solutions. ALP shown by red solid lines, RH shown by green dotted lines and NT shown by blue dashed lines.

the paper, be it for polytropic or isothermal flow.

In fig.(4(a)), the overlap of the parameter spaces for the shock-forming flow corresponding to three different disc models is shown using dark-grey shade. The grey shaded common region has also been demonstrated in the inset of the figure. The figure has been drawn by keeping the values of the black hole spin and the polytropic index of the flow to be fixed. The values of such fixed parameters are shown in the figure. Such values are representative values only, i.e. the shocked flow can be obtained for other set of values of $[a, \gamma]$ as well.

Fig.(4(b)) shows the parameter space diagram spanned by the flow angular momentum and the spin angular momentum of the black hole for a fixed set of values of $[\mathcal{E}, \gamma]$ as specified in the figure. The set of values of $[\mathcal{E}, \gamma]$ is representative and similar $[\lambda, a]$ space can be obtained for other values of $[\mathcal{E}, \gamma]$ as well. We choose the particular set of values $[\mathcal{E} = 1.0001, \gamma = 4/3]$ so that we can cover an extended range of the Kerr parameter to identify the shocked solutions. It is evident from the figure that the lower values of the black hole spin allow shock formation for relatively larger values of flow angular momentum, as well as for a relatively large span of values of the angular momentum. This is probably obvious because a lower spin accretor effectively reduces the influence of the flow angular momentum.

We conclude our discussions on parameter dependence of the shock solutions by studying the role of adiabatic index γ and specific energy \mathcal{E} . Fig.(5) depicts $[\gamma, a]$ space with shock solutions for different values of \mathcal{E} and λ corresponding to the ALP-type of discs. Similar panels can be constructed for NT and RH discs as well, but the trends of variation have been found to be similar. Due to the quality of not being constrained with any truncation radius and thus providing the maximum scope to look for shocks in terms of radial distance,

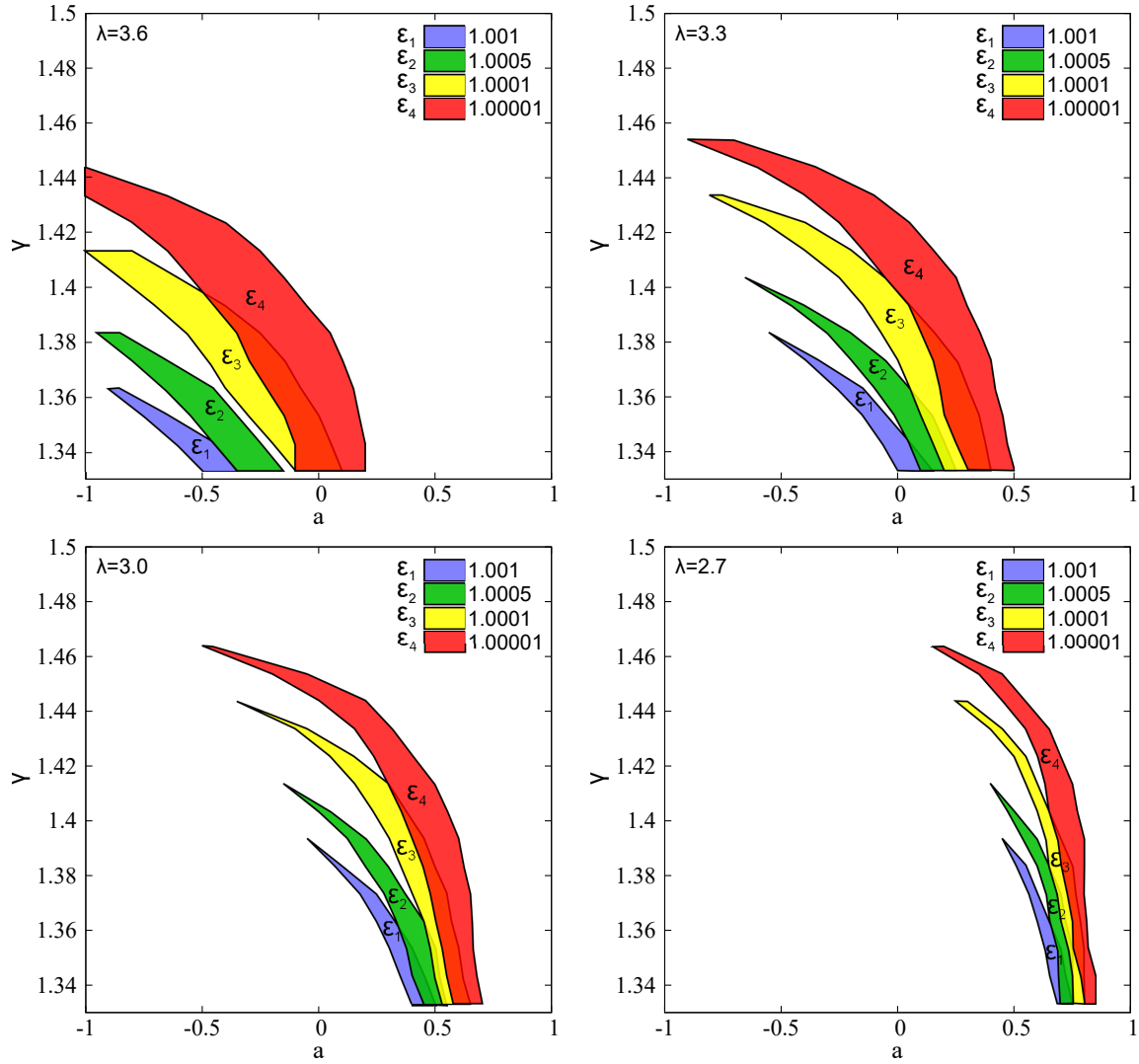


Figure 5: γ - a plot with different \mathcal{E} values ($\mathcal{E}_1 = 1.001$, $\mathcal{E}_2 = 1.0005$, $\mathcal{E}_3 = 1.0001$, $\mathcal{E}_4 = 1.00001$) for (a) $\lambda = 3.6$, (b) $\lambda = 3.3$, (c) $\lambda = 3.0$ and (d) $\lambda = 2.7$.

the ALP disc has been chosen for the purpose of demonstration in this regard.

In fig.(5(a)), we see that the relevant adiabatic indices anti-correlate with the black hole spin parameter. Flows with four different values of specific energy ($\mathcal{E}_1 > \mathcal{E}_2 > \mathcal{E}_3 > \mathcal{E}_4$, values provided in the respective figures and marked with blue, green, yellow and red colours respectively) have been studied. We find that flows with lower values of \mathcal{E} can lead to formation of shocks over a greater range of γ from the fully relativistic limit of $\gamma = 4/3$ till other intermediate values below the non-relativistic limit of $\gamma = 5/3$. The lowest value of \mathcal{E} considered here ($\mathcal{E}_4 = 1.00001$) serves our purpose of explanation. However, even lower values of specific energy can be considered to predict shock solutions theoretically almost over the entire astrophysically relevant range of γ (from fully relativistic to non-relativistic flows). This, of course, comes with an obvious trade-off between the spans of results achieved and the computational costs incurred.

Figs.(5(b)-(d)) shows similar γ vs. a plots with for parameters at which shocks form. The four separate figures (a)-(d) in the panel indicate the successively decreasing values of the flow angular momentum λ . We have already shown in fig.(4(b)) that the flow angular momentum and black hole spin anti-correlate with each other in the context of shock formation. Hence it is expected that as the value of λ is decreased for a given set of $[\mathcal{E}, \gamma]$, shocks will be obtained at higher values of a . That is exactly what we see along figs.(5(b)-(d)). However, it should also be noted that the range of a over which such solutions are obtained decreases significantly with decreasing flow angular momentum. The inter-relationships between all the system parameters are extremely complex for such highly non-linear systems. A definitive picture can only be procured through generation of a complete 4-dimensional parameter space diagram. Scanning the entire possible parameter space is heavily time-consuming and computationally exhausting, and hence is beyond our present theoretical scope. However, an integrated study of various parameter combinations as presented in our work, provides a sufficiently comprehensive assessment of the relevant shock regimes.

In fig.(6(a)), we plot the shock locations (measured from the horizon in units of the Schwarzschild radius $R_g (= 2GM_{BH}/c^2)$), and other shock-related quantities as a function of the black hole spin for three different disc models. The set of values of $[\mathcal{E}, \lambda, \gamma]$ are kept fixed, and their fixed values are shown in the respective figures.

We observe that the shock location (r_{sh}) co-relates with the spin parameter of the black hole. This is intuitively obvious because higher spin effectively enhances the effect of flow angular momentum. Greater the angular momentum, larger will be the distance at which the centrifugal barrier forms. The shock under consideration is centrifugal pressure-supported. Hence, r_{sh} is pushed farther away from the horizon with increasing values of a . For fixed values of $[\mathcal{E}, \lambda, \gamma, a]$ the shock forms farthest for ALP-type of disc, whereas it forms closest for RH discs. For NT-type discs, the shock forms at an intermediate distance. r_{sh} vs. a curve for ALP-type discs approaches that for NT-type discs asymptotically but they never intersect. This has been investigated for values of $[\mathcal{E}, \lambda, \gamma, a]$ other than those used to generate fig.(6). With decreasing λ , the overall set of r_{sh} - a curves shift towards higher values along the a and r_{sh} axes. Thus, we find that r_{sh} anti-correlates with λ as expected since r_{sh}

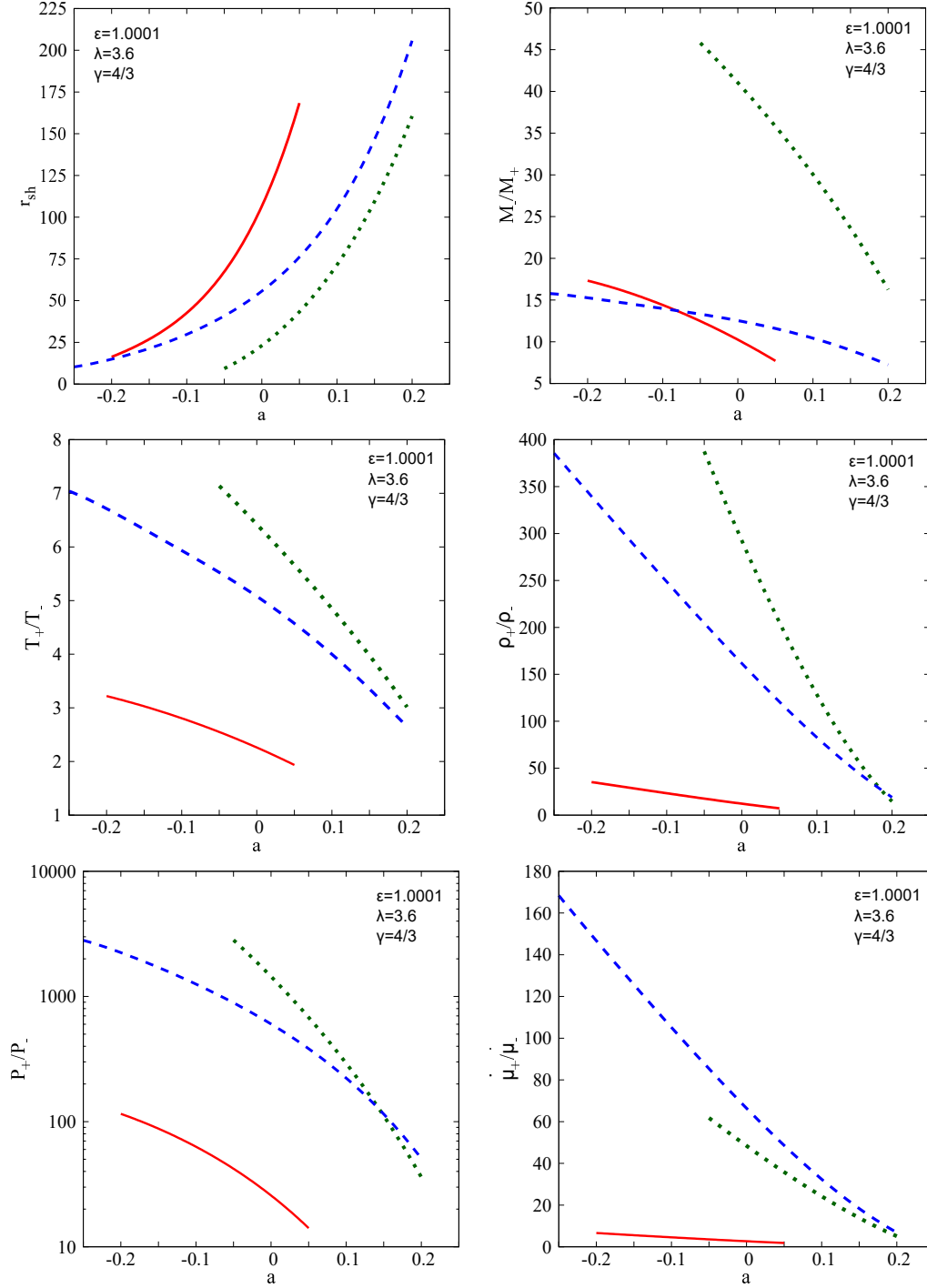


Figure 6: Shock location - (a) r_{sh} (in terms of R_g) vs. a , Ratios at shock - (b) M_-/M_+ vs. a , (c) T_+/T_- vs. a , (d) ρ_+/ρ_- vs. a , (e) P_+/P_- vs. a and (f) μ_+/μ_- vs. a . ‘-’ and ‘+’ refer to values ‘before’ and ‘after’ the shock respectively. ALP shown by red solid lines, RH shown by green dotted lines and NT shown by blue dashed lines.

co-relates with a and a anti-correlates with λ . Similarly, the authors have verified that r_{sh} anti-correlates with γ and co-relates with \mathcal{E} (since γ anti-correlates and \mathcal{E} co-relates with a , as shown in fig.(5)).

At the shock location, directed flow velocity gets randomized and the gravitational potential energy available at the shock location determines the shock strength. The closer the shock forms to the horizon, the stronger it should be. Hence the strength should anti-correlate with the shock location and thus with the black hole spin parameter. This is exactly what we observe in fig.(6(b)). The shock strength is defined as the ratio of the pre- to post-shock Mach number of the flow. We plot the shock strength (M_-/M_+ , hereafter any accretion variable with a subscript ‘-’ would indicate that it has been measured at the shock location before the shock is formed, i.e. it has been measured on the integral solution passing through the outer sonic point, and variables with subscript ‘+’ would refer to the post-shock values measured at the shock location on the integral solution passing through the inner sonic point) as a function of the Kerr parameter for both prograde and retrograde flow. As argued above, we clearly see that the shock strength anti-correlates with the black hole spin for both co-rotating as well as counter-rotating flows. We observe an intersection of the M_-/M_+ vs. a curve for the ALP and NT disc models. Such intersection, by any means, does not indicate any degeneracy in the disc models, i.e. it does not mean that for certain values of $[\mathcal{E}, \lambda, \gamma, a]$, two or more separate disc models provide the same value of any significant accretion variable. It is important to note that the ratio of Mach numbers can assume same values at the point of intersection, but not the value of any individual quantity. The ratio of Mach numbers can be the same for two (or more) different set of post-shock values. The shock strength is found to co-relate with λ and γ , and anti-correlate with \mathcal{E} as expected from the relation between the corresponding parameters with a shown previously in the respective parameter-space diagrams. In fig.(6(c)) and (6(d)), the post- to pre-shock temperature and shock compression ratio (ratio of flow densities after and before the shock) have been plotted against the change of black hole spin. As expected, these quantities anti-correlate with a , because greater the amount of available gravitational potential energy at the shock, higher will be the amount of temperature changes and larger will be the amount of compression. It is evident from the figure that the RH-type of discs become most dense and hot after the shock forms. Whereas, the ALP-type of discs change their temperature and density in minimum amounts at the shock. The NT kind of flow assumes an intermediate value for these two ratios. More or less, similar trends are observed for the variation of the ratio of the post to the pre-shock fluid pressure for three different disc models. Here too, we find intersection among the two curves, but as explained earlier, it does not indicate any type of degeneracy. Finally, in fig.(6(f)) we plot the ratio of the post to pre-shock entropy accretion rates for three disc models as a function of the black hole spin. The ratio of the entropy accretion rate is a measure of entropy production at the shock. As we observe, such measure may not have any one-to-one correspondence with the shock strength. The entropy is directly related to the expression of the mass accretion rate of the steady-state flow.

In passing, we would like to mention that the set of $[\mathcal{E}, \lambda, \gamma]$ used to draw this figure is not unique by any means. We chose this set of values just to have a reasonable span of the black hole spin covering both prograde as well as retrograde flows. It is to be noted that shock

does form for accreting black holes with intermediate as well as higher spin, for both co- and counter-rotating flows. One can obtain shocked flows for high-spin accretors using a suitable set of $[\mathcal{E}, \lambda, \gamma]$.

4 Isothermal accretion

4.1 Fluid equations

The equation of state characterising isothermal fluid flow is given by,

$$p = c_s^2 \rho = \frac{\mathcal{R}}{\mu} \rho T = \frac{k_B \rho T}{\mu m_H} \quad (49)$$

where T is the bulk ion temperature, \mathcal{R} is the universal gas constant, k_B is Boltzmann constant, m_H is mass of the Hydrogen atom and μ is the mean molecular mass of fully ionized hydrogen. The temperature T as introduced in the above equation, and which has been used as one of the parameters to describe the isothermal accretion, is the temperature-equivalent of the bulk ion flow velocity. That is the reason why the value appears to be high ($10^{10} - 10^{11}$ K) in this work. The actual disc temperature is the corresponding electron temperature, which should be of the order of $10^6 - 10^7$ Kelvin. Now using the equation of state (49), the equations needed to draw the phase portrait will be derived.

4.1.1 Energy-momentum equation

Using eqn. (49), eqn. (13) can be rewritten as

$$u^\nu \left[D_\nu (\rho c_s^2 u_\mu) - D_\mu (\rho c_s^2 u_\nu) \right] = 0 \quad (50)$$

Using the time component of this equation and the stationary nature of the flow one obtains the conserved quantity

$$\xi = v_t \rho c_s^2. \quad (51)$$

Taking the logarithmic derivative of eqn. (51), the derivative of density ρ' is obtained as

$$\frac{\rho'}{\rho} = \frac{u'}{u(u^2 - 1)} - \left(\frac{f'}{f} + \frac{\Delta'}{2\Delta} \right) \quad (52)$$

4.1.2 Continuity equation

In this section we again derive the velocity gradient for two separate classes, one consisting of NT and RH and the other consisting of the ALP height prescription. We note that we can still integrate continuity equation and the conserved quantity mass accretion rate \dot{M} as defined in eqn. (23).

NT & RH discs Using the fact that $\frac{v}{\rho}$ is the constant c_s^2 , the height of the disc for these two height prescriptions in case of isothermal accretion can be written as

$$H(r) = c_s f(r, a) \quad (53)$$

Using eqn. (53) and putting the value of $\frac{v}{\rho}$ in the logarithmic derivative of eqn. (23), we obtain

$$\frac{du}{dr} = \frac{u(1-u^2) \left[c_s^2 \left(\frac{\Delta'}{2\Delta} + \frac{f'}{f} \right) + \frac{1}{2} \left(\frac{B'}{B} - \frac{\Delta'}{\Delta} \right) \right]}{u^2 - c_s^2} = \frac{N}{D}. \quad (54)$$

Again we mention that for NT height recipe, $f(r, a)$ is replaced by $f_{NT}(r, a)$ as defined in eqn. (27) and for RH height recipe, we replace $f(r, a)$ by $f_{RH}(r, a)$ as defined in eqn. (6).

ALP discs For this recipe, the height function in the case of isothermal accretion is

$$H(r) = c_s^2 \sqrt{\frac{2r^4}{\lambda^2 v_t^2 - a^2(v_t - 1)}}. \quad (55)$$

Following the same procedure as used in previous class of height recipes, one yields

$$\frac{du}{dr} = \frac{c_s^2 \left(\frac{\Delta'}{2\Delta} + \frac{2}{r} - (2\lambda^2 v_t - a^2) \frac{v_t P}{4F} \right) - \frac{P}{2}}{\frac{u}{1-u^2} - \frac{c_s^2}{u(1-u^2)} (1 - (2\lambda^2 v_t - a^2) \frac{u^2 v_t}{2F})} \quad (56)$$

where $P = \frac{\Delta'}{\Delta} - \frac{B'}{B}$ and $F = \lambda^2 v_t^2 - a^2(v_t - 1)$.

4.2 Critical point conditions

Following the same scheme as in polytropic process, we find the slopes of directrices at critical points, solve for the radial position of critical point, r_c and draw the phase portrait. Again we present NT and RH-type of discs in the first class and ALP-type of discs in the next class for reasons stated earlier.

4.2.1 NT & RH discs

Setting $D = 0$ in Eq. (54) yields

$$u^2|_c = c_s^2|_c \quad (57)$$

Setting $N = 0$ yields

$$c_s^2|_c = \frac{\frac{\Delta'}{\Delta} - \frac{B'}{B}}{\left(\frac{\Delta'}{2\Delta} + \frac{f'}{f} \right)}. \quad (58)$$

To find the critical points for isothermal accretion the method followed is different from that of polytropic accretion as the basic parameter characterising the flow is different for

polytropic and isothermal accretion. In polytropic accretion, the parameters are \mathcal{E} and λ , whereas the isothermal flow is characterized by the parameters T and λ . So, by putting the chosen value of the temperature T in Eq. (49) to find the constant sound speed. The value of c_s^2 is used in Eq. (58) and the equation

$$\frac{\mathcal{R}}{\mu} T = \frac{\frac{\Delta'}{\Delta} - \frac{B'}{B}}{\left(\frac{\Delta'}{2\Delta} + \frac{f'}{f}\right)} \quad (59)$$

The right hand side of eq. (59) is function of the variable r and by solving this equation the critical points are obtained.

The two values of the slopes at critical point is obtained from the quadratic equation

$$\alpha_1 \left(\frac{du}{dr}\right)^2 - \alpha_2 \left(\frac{du}{dr}\right) - \alpha_3 = 0 \quad (60)$$

where,

$$\alpha_1 = 4u_c \quad (61)$$

$$\alpha_2 = \left(\frac{B'}{B} - \frac{\Delta'}{\Delta} + \left(\frac{\Delta'}{\Delta} + \frac{2f'}{f}\right)u_c^2\right) (1 - 3u_c^2) \quad (62)$$

$$\alpha_3 = u_c (1 - u_c^2) \left[2u_c^2 \left(\frac{\Delta''}{2\Delta} + \frac{f''}{f} - \frac{1}{2} \left(\frac{\Delta'}{\Delta}\right)^2 - \frac{f'^2}{f}\right) - \frac{\Delta''}{\Delta} + \frac{B''}{B} + \left(\frac{\Delta'}{\Delta}\right)^2 - \left(\frac{B'}{B}\right)^2 \right] \quad (63)$$

Thus we are equipped with all the information needed to draw the phase portrait diagram for a given parameter set of $[T, \lambda, a]$.

4.2.2 ALP discs

The critical point conditions obtained by setting $N = 0$ and $D = 0$ are:

$$u_c^2|_{VE} = \frac{P1}{\frac{\Delta'}{\Delta} + \frac{4}{r}} \quad (64)$$

$$c_{sc}^2|_{VE} = \frac{u_c^2}{1 - \frac{u_c^2 v_t (2\lambda^2 v_t - a^2)}{2F}} \quad (65)$$

Velocity gradient at critical points:

$$\left(\frac{du}{dr}\right)_c|_{VE} = -\frac{\beta_{VE}}{2\alpha_{VE}} \pm \frac{1}{2\alpha_{VE}} \sqrt{\beta_{VE}^2 - 4\alpha_{VE}\Gamma_{VE}} \quad (66)$$

where,

$$\alpha_{VE} = \frac{1+u_c^2}{(1-u_c^2)^2} - D_2 D_6, \quad \beta_{VE} = D_2 D_7 + \tau_4, \quad \Gamma_{VE} = -\tau_3,$$

$$\begin{aligned}
D_2 &= \frac{c_s^2}{u(1-u^2)} (1 - D_3), \quad D_6 = \frac{3u^2-1}{u(1-u^2)} - \frac{D_5}{1-D_3}, \\
D_7 &= \frac{D_3 D_4 v_t P_1}{2(1-D_3)}, \quad \tau_3 = \left(c_s^2 \tau_2 - c_s^2 v_5 v_t \frac{P_1}{2} \right) - \frac{P_1'}{2}, \\
\tau_4 &= \frac{c_s^2 v_5 v_t u}{1-u^2}, \quad v_1 = \frac{\Delta'}{2\Delta} + \frac{2}{r} - (2\lambda^2 v_t - a^2) v_t \frac{P_1}{4F}, \\
D_3 &= \frac{u^2 v_t (2\lambda^2 v_t - a^2)}{2F}, \quad D_4 = \frac{1}{v_t} + \frac{2\lambda^2}{2\lambda^2 v_t - a^2} - \frac{2\lambda^2 v_t - a^2}{F}, \quad D_5 = D_3 \left(\frac{2}{u} + \frac{D_4 v_t u}{1-u^2} \right), \quad \tau_2 = \tau_1 - \frac{v_t (2\lambda^2 v_t - a^2)}{4F} P_1', \\
v_5 &= (2\lambda^2 v_t - a^2) \frac{P_1}{4F} v_4, \\
\tau_1 &= \frac{1}{2} \left(\frac{\Delta''}{\Delta} - \frac{(\Delta')^2}{\Delta^2} \right) - \frac{2}{r^2}, \quad v_4 = \frac{v_3}{(2\lambda^2 v_t - a^2) F}, \quad v_3 = (4\lambda^2 v_t - a^2) F - (2\lambda^2 v_t - a^2)^2 v_t.
\end{aligned}$$

The location of critical points are solved just as described before by putting appropriate T in eq. (49) and then solving eq. (65) by using the corresponding value of c_s .

4.3 Parameter space

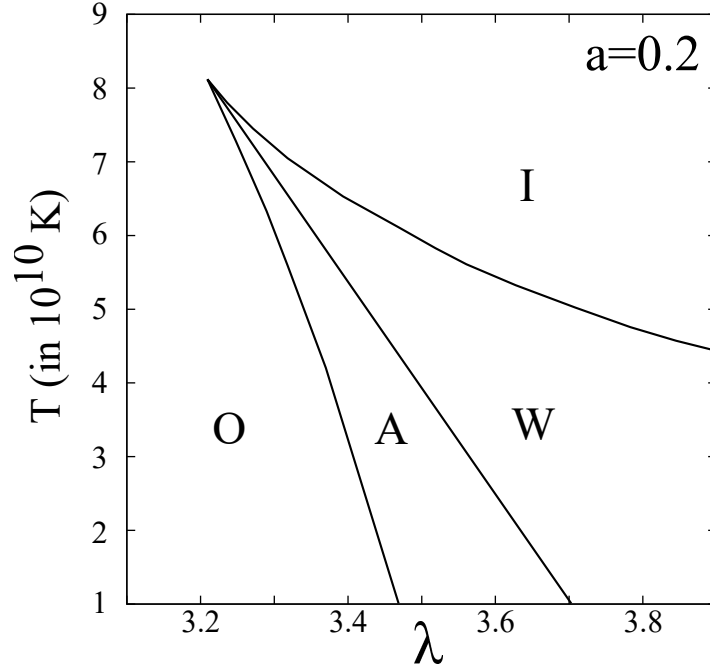


Figure 7: $T - \lambda$ parameter space plot for accretion and wind in isothermal NT disc at $a = 0.2$

In fig.(7), we show that the parameter space spanned by the (constant) bulk flow temperature and the flow angular momentum for a particular value of the black hole spin ($a = 0.2$). Similar diagrams can be produced for other values of a , both for prograde as well as retrograde flows. As discussed in section 3.3, the parameter space is divided into four different regions, O , I , A and W as shown in the figure. The parameter space has been constructed for discs with NT-type of flow thickness.

Both regions O and I produce a single sonic (critical) point. For O , the sonic point is outertype, i.e. it forms far away from the horizon. Whereas for I , it is inner-type, i.e. it forms very close to the horizon. Parameter space region marked by A designates accretion flow with three critical points. If shock forms, then the largest (outermost) and smallest (innermost)

critical points may become sonic points and two different integral accretion solutions, passing through the outermost and the innermost critical (sonic) points respectively, may be joined using a stationary shock solution. For flow characterised by parameters chosen from region A , the quasi-specific energy measured along the integral accretion solution passing through the inner sonic point is less than the same measured along the solution passing through the outer sonic point ($\xi(r_c^{in}) < \xi(r_c^{out})$). The situation is just opposite for flows characterised by parameters taken from the region W . When parameters are taken from region W , the accretion flow can pass through only one sonic point, however the wind (outgoing) solutions can have three critical points. Outgoing solutions passing through the inner and the outer critical points may be joined through a stationary shock. We will, however, not discuss multi-transonic shocked wind in the present work.

4.4 General relativistic isothermal shock conditions

We note that $h = 1$ for isothermal process, which in turns yield,

$$T^{rr} = \rho \left((v^r)^2 + c_s^2 g^{rr} \right) \quad (67)$$

NT & RH discs In this case the shock-invariant quantity turns out to be

$$S_{sh} = \frac{(u^2(1 - c_s^2) + c_s^2)}{u\sqrt{1 - u^2}} \quad (68)$$

where we have removed any over all factor of r as shock invariant quantity is to be evaluated at $r = r_{sh}$ for different branches of flow.

ALP discs In this case, the shock-invariant quantity turns out to be

$$S_{sh} = \frac{(u^2(1 - c_s^2) + c_s^2)\sqrt{\lambda^2 v_t^2 - a^2(v_t - 1)}}{u\sqrt{1 - u^2}} \quad (69)$$

where v_t is given in (8).

We show the multi-transonic flow topology with shock for a set of $[T, \lambda, a]$ as specified in the diagram. We also show the segregated disc structure (the edge-on view in fig.(8(a)), and the face-on view in fig.(8(c))) for various subsonic and supersonic parts of the flow, as clarified in much detail in section 3.4 while describing features of fig.(2). There is, however, a major difference between post-shock disc structure in polytropic flow with energy-preserving shock and for isothermal flow with temperature-preserving shock. We have seen that for polytropic shocked accretion, lack of dissipation of energy increases the post-shock flow temperature and the post-shock part of the disc expands to produce a torus-kind of geometry. For isothermal shock, however, the thermal energy generated at the shock is allowed to liberate in order to maintain invariance of the flow temperature. Since no additional thermal energy gets trapped, the post-shock disc, unlike its polytropic counterpart, does not get puffed-up. The energy liberated at the shock may power the strong flares emanating out of the axisymmetric accretion around supermassive black holes at the centre of the galaxies. We shall elaborate

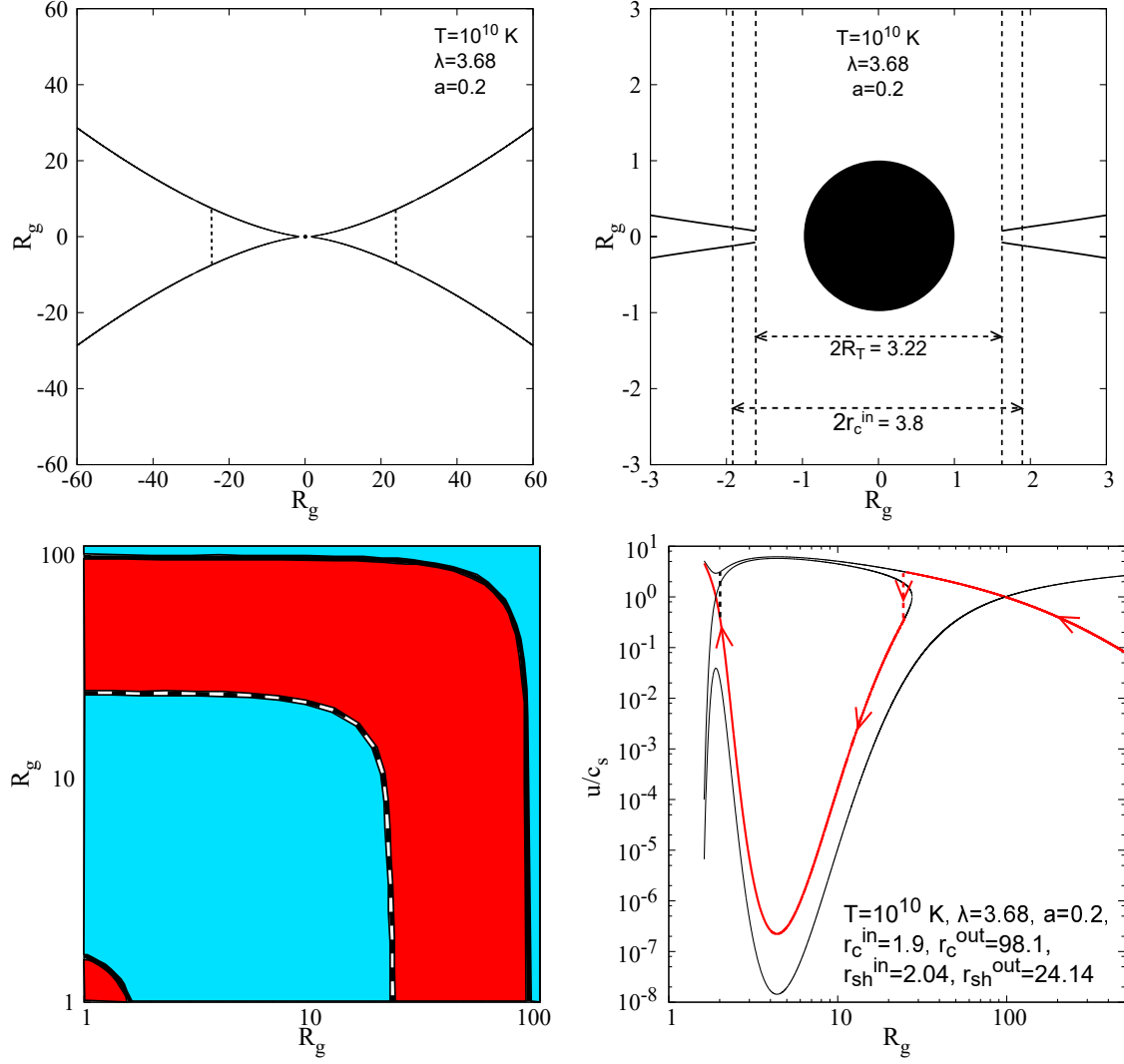


Figure 8: Isothermal NT disc - (a) Disc height vs. radial distance (in units of R_g) with vertical dotted lines depicting the shock locations ($r_{sh} = 24.15$). (b) Magnified view of the central region depicting the truncation radius (R_T) and inner critical point (r_c^{in}). (c) Face-on view of the disc (Solid curves represent sonic points and dashed curve represents shock front. Regions shaded in cyan and red depict subsonic and supersonic flows respectively). (d) Mach number vs. radial distance profile (red path depicts physical flow in the direction indicated with arrows).

this aspect in subsequent sections. In fig.(8(b)), the innermost part of the disc has been shown separately along with the termination radius (R_T) of the disc.

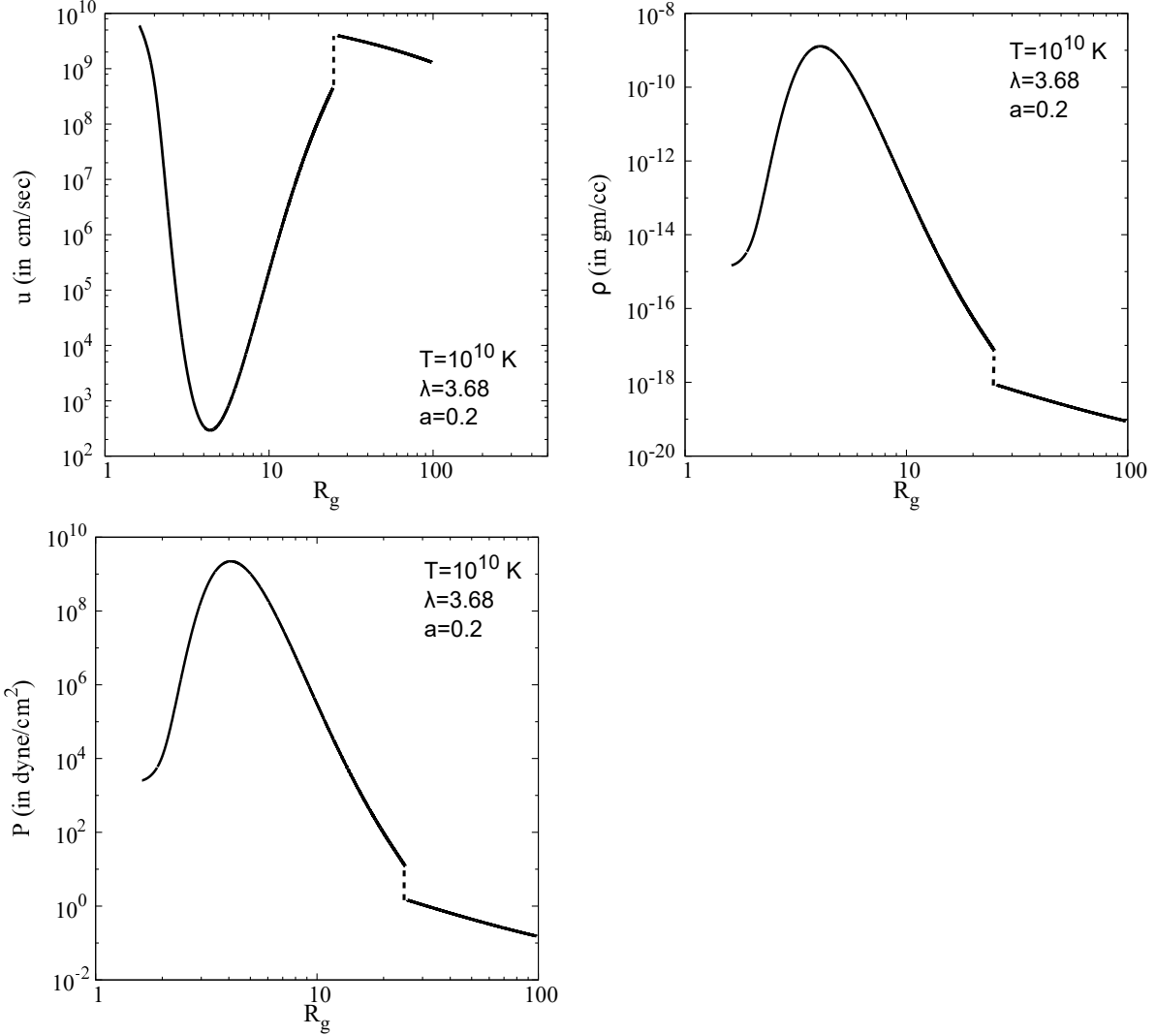


Figure 9: Isothermal NT flow profile - (a) Advective flow velocity (u) vs r . (b) Rest mass density (ρ) vs. r . (c) Pressure (P) vs. r . u in units of cm/sec, ρ in units of gm/cc, P in units of dyn/cm², r in units of R_g .

Fig.(9) shows the variation of the dynamical velocity u , the matter density ρ and the fluid pressure P , as a function of the radial distance (measured from the horizon) for the shocked branch. The vertical dashed line signifies the discontinuous shock transition which joins the pre-shock flow solution passing through the outer sonic point with the post-shock flow solution passing through the inner sonic point. For isothermal accretion, the sound speed remains invariant, hence the Mach number profile turns out to be just a scaled down version of the velocity profile.

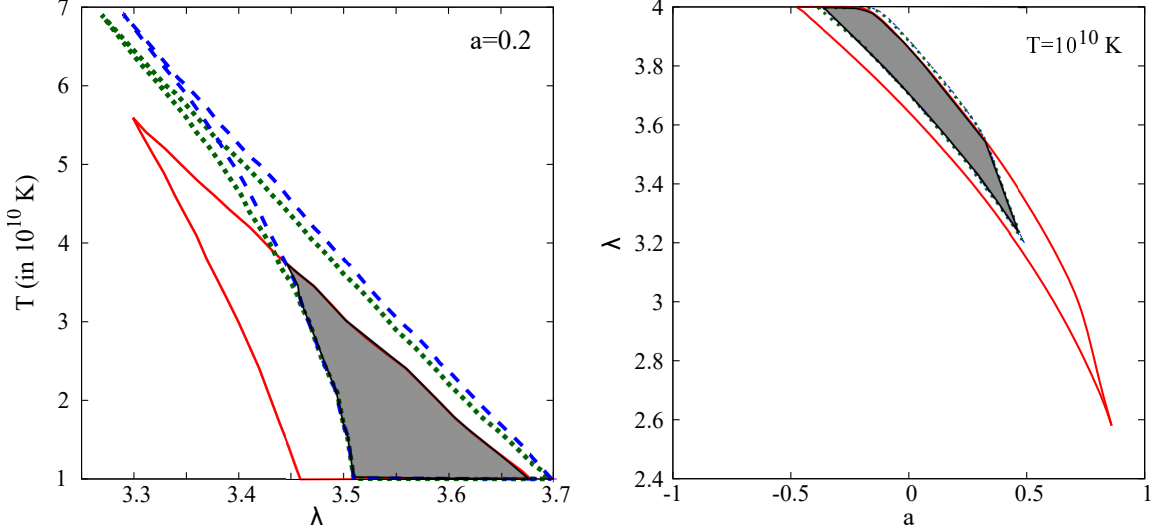


Figure 10: Parameter space for shocked accretion flows - (a) Flow temperature (T) vs. λ ($a = 0.2$). (b) λ vs. a ($T = 10^{10} K$). Solid red curves, green dotted curves and blue dashed curves represent ALP, RH and NT discs respectively. Shaded regions depict overlap zones for the three disc models.

Fig.(10(a)) shows the parameter space (spanned by the flow temperature and flow angular momentum) for multi-transonic shocked flow for three different disc thicknesses as considered in our work. The figure has been obtained for a fixed value of black hole spin $a = 0.2$. Similar figures can be obtained for any other value of a for both prograde as well as retrograde flows. The region of parameter space common to all three disc thicknesses has been shaded in dark grey colour.

The parameter space spanned by the flow angular momentum λ and the black hole spin a has been depicted in fig.(10(b)), for a fixed value of flow temperature $T = 10^{10}$ K. This value is only representative and similar diagrams with the same general features can be obtained for other values of T as well. The particular value of T has been chosen to cover an extended range of a allowing shock solutions. Similar to the polytropic case (fig.(4(b))), lower values of the Kerr parameter permit shock formation for flows with higher values of the specific angular momentum.

Fig.(11(a)) shows the variation of shock location with the black hole spin for both the co-rotating as well as counter-rotating flows. Faster rotating black holes produce the shock at larger distances for prograde flow whereas the trend is reverse in case of retrograde accretion. It should be noted that the NT and RH-type discs produce shocks in extremely nearby locations for isothermal flows. Similar conclusions drawn while observing the variation of the ratios of the pre-(post-) to the post-(pre-) shock accretion variables as a function of the Kerr parameter. Such variations are shown in fig.(11(b-d)). The shock becomes stronger and the post-shock flow becomes denser, as the shock location approaches towards the horizon. This is physically consistent as larger amounts of gravitational potential energy will be available

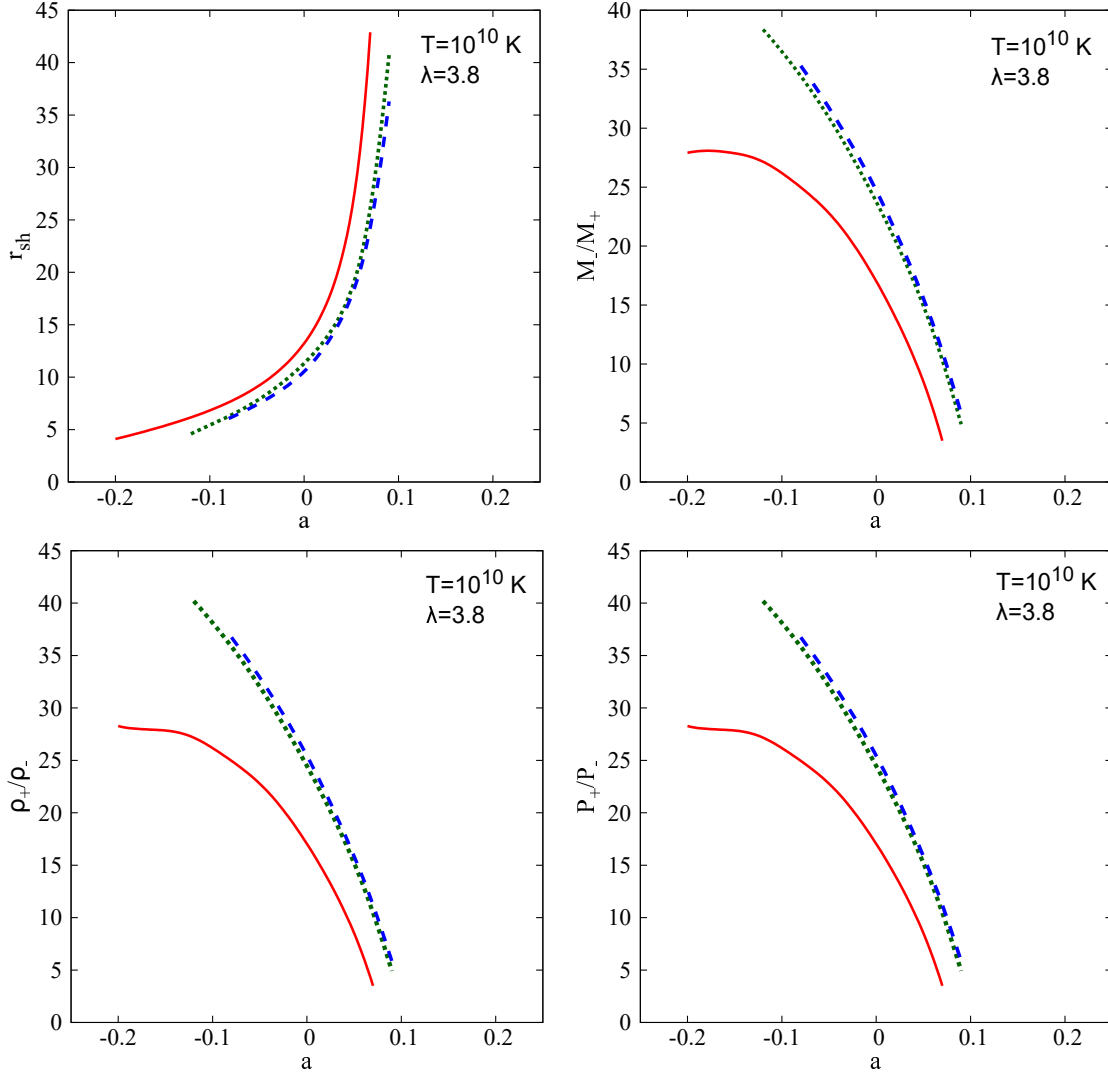


Figure 11: Shock location - (a) r_{sh} (in terms of R_g) vs. a , Ratios at shock - (b) M_-/M_+ vs. a , (c) ρ_+/ρ_- vs. a and (d) P_+/P_- vs. a . ‘-’ and ‘+’ refer to ‘before’ and ‘after’ shock respectively. ALP shown by red solid lines, RH shown by green dotted lines and NT shown by blue dashed lines.

for liberation when shock forms closer to the horizon. The results have been obtained for a particular set of $[T, \lambda]$. But results with the same variational trends can be obtained for any other relevant values of the given flow parameters.

4.5 Energy dissipation at temperature-preserving shock

The quasi-specific energy ξ plays a role similar to that played by entropy accretion rate $\dot{\Xi}$ for polytropic flow. ξ decreases after the flow encounters a shock. The difference of values of ξ computed along the integral accretion solutions passing through the outer and the inner sonic points, respectively, is a measure of the flow energy liberated at shock. Such energy liberation mechanism may explain the formation and dynamics of flares (as observed in various wavelengths) emanating out from the proximity of our own Galactic Centre black hole.

In fig.(12), we plot the ratio of the pre- to post- shock values of ξ as a function of the Kerr parameter. As a reference, we also show the variation of corresponding shock locations with the black holes spin. Three sets of figures have been produced for three different values of the flow angular momentum λ and for the same value of the temperature as shown in the figure.

We expect that the ratio of ξ at shock might anti-correlate with the shock location r_{sh} , since for smaller values of r_{sh} (forming closer to the horizon, in a relatively stronger gravity regime), the gravitational potential energy available for liberation is higher. Also, values of the effective centrifugal barrier, i.e. $(\lambda \pm a)$ determine the amount of energy dissipated at the shock. For lower values of $(\lambda \pm a)$, accretion flow has larger values of the radial advective velocity. This velocity is directed, and gets randomised at the shock. The larger the value of the directed bulk velocity, the higher is the amount of energy liberated when it gets randomised through shock formation. The value of the ratio of the pre- to post-shock quasi-specific energy, should, thus anti-correlate with λ , as well as with $(\lambda \pm a)$.

This is exactly what we observe in the figure (see three consecutive panels a–c in fig.(12)). We also see that the amount of energy liberated can be as large as (approximately) 9%. Thus the disc may become considerably luminous (on the corresponding wavelength) at the shock, and can also produce a radiatively efficient post-shock flow. It has been found (see the figures) that among the three different disc-height recipes, the NT-type of disc liberates maximum amount of energy, and hence becomes maximally luminous at the shock, provided the initial set of boundary conditions remain the same.

It also requires to be mentioned that the aforementioned energy-liberation process is not similar to the Blandford-Znajek (BZ) mechanism ([Blandford and Znajek, 1977]), where the rotational energy of the black hole is extracted to power jets. BZ mechanism requires the presence of poloidal magnetic field lines around a spinning black hole, which extracts the rotational energy of the hole itself. On the contrary, our simple theoretical model of purely general relativistic hydrodynamic flow does not include any magnetic energy component. The energy-liberation mechanism discussed in our work is not similar to the Penrose process ([Penrose and Floyd, 1971]) as well, since in our model, energy gets liberated at the shock

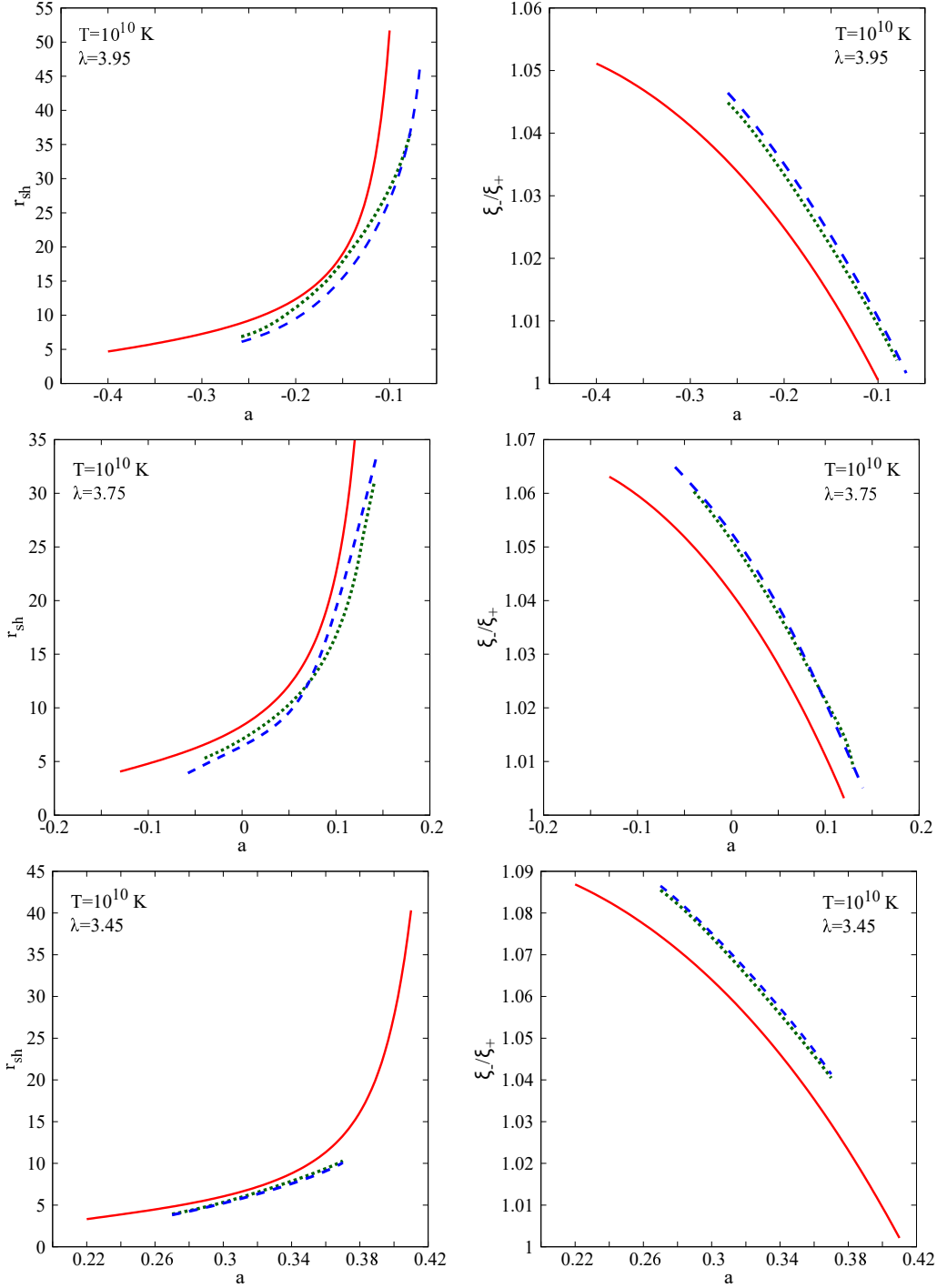


Figure 12: Energy dissipation at shock - ξ_-/ξ_+ vs. a along with the corresponding r_{sh} (in terms of R_g) vs. a for $T = 10^{10}$ K and (a) $\lambda = 3.95$, (b) $\lambda = 3.75$ and (c) $\lambda = 3.45$. ‘-’ and ‘+’ represent quantities ‘before’ and ‘after’ shock respectively. ALP shown by red solid lines, RH shown by green dotted lines and NT shown by blue dashed lines.

location residing well outside the ergosphere.

Acknowledgement

PT would like to acknowledge the kind hospitality provided by Harish-Chandra Research Institute, HBNI, Department of Atomic Energy, Government of India, for supporting his visit through the plan budget of Cosmology and High Energy Astrophysics grant.

References

- H. Abraham, N. Bilić, and T. K. Das. *Class. & Quant. Grav.*, 23:2371, 2006.
- M. A. Abramowicz and S. K. Chakrabarti. *ApJ*, 350:281, 1990.
- M. A. Abramowicz and S. Kato. *ApJ*, 336:304, 1989.
- M. A. Abramowicz and W. H. Zurek. *ApJ*, 246:314, 1981.
- M. A. Abramowicz, A. Lanza, and M. J. Percival. *ApJ*, 479:179, 1997.
- D. B. Ananda, S. Bhattacharya, and Tapas K. Das. *Gen. Rel. & Grav.*, 47:96, 2015. doi: 10.1007/s10714-015-1940-2.
- P. Barai, T. K. Das, and P. J. Wiita. *ApJL*, 613:L49–L52, 2004.
- V. S. Beskin. *Phys.-Usp.*, 40:659, 1997.
- V. S. Beskin. *MHD Flows in Compact Astrophysical Objects: Accretion, Winds and Jets*. Springer, 2009.
- V. S. Beskin and A. Tchekhovskoy. *A & A*, 433:619, 2005.
- N. Bilić, A. Choudhary, T. K. Das, and S. Nag. *Class. & Quant. Grav.*, 31:35002, 2014.
- A. A. Bisikalo, V. M. Boyarchuk, V. M. Chechetkin, O. A. Kuznetsov, and D. Molteni. *MNRAS*, 300:39, 1998.
- O. Blaes. *MNRAS*, 227:975, 1987.
- R. D. Blandford and R. L. Znajek. *MNRAS*, 179:433–456, 1977. doi: 10.1093/mnras/179.3.433.
- D. A. Bollimpalli, S. Bhattacharya, and T. K. Das. *New Astron.*, 51:153–160, 2017. doi: 10.1016/j.newast.2016.09.001.
- R. H. Boyer and R. W. Lindquist. *J. Math. Phys.*, 8:265, 1967.
- H. J. Bussemaker, D. Thirumalai, and J. K. Bhattacharjee. *Phys. Rev. Lett.*, 79(3):3, 1997.

- S. K. Chakrabarti. *ApJ*, 347:365, 1989.
- S. K. Chakrabarti. *ApJ*, 471:237, 1996.
- S. K. Chakrabarti. *MNRAS*, 283:325, 1996. doi: 10.1093/mnras/283.1.325.
- S. K. Chakrabarti and S. Das. *MNRAS*, 327:808, 2001.
- B. Czerny, M. Mościbrodzka, D. Proga, T. K. Das, and A. Siemiginowska. In S. Hledík and Z. Stuchlík, editors, *Proceedings of RAGtime 8/9: Workshops on Black Holes and Neutron Stars*, pages 35–44, 2007.
- T. K. Das. *ApJ*, 577:880–892, 2002. doi: 10.1086/342114.
- T. K. Das and B. Czerny. *MNRAS*, 421:L24–L28, 2012. doi: 10.1111/j.1745-3933.2011.01199.x.
- T. K. Das and B. Czerny. *New Astron.*, 17:254, 2012.
- T. K. Das, J. K. Pendharkar, and S. Mitra. *ApJ*, 592:1078, 2003.
- T. K. Das, S. Nag, S. Hegde, S. Bhattacharya, I. Maity, B. Czerny, P. Barai, P. J. Wiita, V. Karas, and T. Naskar. *New Astron.*, 37:81, 2015.
- S. Datta and T. K. Das. *arXiv e-prints*, art. arXiv:1910.06768, 2019.
- S. Datta, M. A. Shaikh, and T. K. Das. *New Astron.*, 63:65 – 74, 2018. doi: <https://doi.org/10.1016/j.newast.2018.03.003>.
- S. W. Davis and I. Hubeny. *Apj Suppl.*, 164:530, 2006.
- I. K. Dihingia, S. Das, D. Maity, and S. Chakrabarti. *Phys. Rev. D.*, 98(8):083004, 2018. doi: 10.1103/PhysRevD.98.083004.
- I. K. Dihingia, S. Das, D. Maity, and A. Nandi. *MNRAS*, 488(2):2412–2422, 2019a. doi: 10.1093/mnras/stz1933.
- I. K. Dihingia, S. Das, and A. Nandi. *MNRAS*, 484(3):3209–3218, 2019b. doi: 10.1093/mnras/stz168.
- C. Eckart. *Phys. Rev.*, 58:919–924, 1940. doi: 10.1103/PhysRev.58.919.
- K. Ferrière. *A & A*, 505:1183–1198, 2009. doi: 10.1051/0004-6361/200912617.
- J. Fukue. *PASJ*, 35:355, 1983.
- J. Fukue. *PASJ*, 39:309, 1987.
- J. Fukue. *PASJ*, 56:681, 2004a.
- J. Fukue. *PASJ*, 56:959, 2004b.

- J. Fukue. *MNRAS*, 483(3):3839–3850, 2019. doi: 10.1093/mnras/sty3380.
- K. Fukumara and S. Tsuruta. *ApJ*, 611:964, 2004.
- K. Fukumura, M. Takahashi, and S. Tsuruta. *ApJ*, 657(1):415–427, 2007. doi: 10.1086/510660.
- C. F. Gammie and R. Popham. *ApJ*, 498:313, 1998.
- R. Genzel, F. Eisenhauer, and S. Gillessen. *Rev. Mod. Phys.*, 82:3121–3195, 2010. doi: 10.1103/RevModPhys.82.3121.
- A. M. Ghez, S. Salim, N. N. Weinberg, J. R. Lu, T. Do, J. K. Dunn, K. Matthews, M. R. Morris, S. Yelda, E. E. Becklin, T. Kremenek, M. Milosavljevic, and J. Naiman. *ApJ*, 689:1044–1062, 2008. doi: 10.1086/592738.
- S. Gillessen, F. Eisenhauer, T. K. Fritz, H. Bartko, K. Dodds-Eden, O. Pfuhl, T. Ott, and R. Genzel. *ApJ*, 707:L114–L117, 2009. doi: 10.1088/0004-637X/707/2/L114.
- S. Hacyan. *Gen. Rel. & Grav.*, 14(4):399–410, April 1982. doi: 10.1007/BF00756273.
- R. C. Hilborn. *Chaos and Nonlinear Dynamics: An Introduction for Scientists and Engineers*. Oxford University Press, 2001.
- L. C. Ho. *Observational Evidence For Black Holes in the Universe*, ed. Chakrabarti, S. K. Dordrecht: Kluwer, 1999.
- I. Hubeny and V. Hubeny. *ApJ*, 505:585, 1998.
- I. V. Igumenshchev and M. A. Abramowicz. *MNRAS*, 303:309, 1999.
- A. F. Illarionov. *Soviet Astron.*, 31:618, 1988.
- A. F. Illarionov and R. A. Sunyaev. *A & A*, 39:205, 1975.
- D. W. Jordan and P. Smith. *Nonlinear Ordinary Differential Equations*. Oxford University Press, Oxford, 1999.
- M. Kafatos and R. X. Yang. *MNRAS*, 268:925, 1994.
- G. D. Karssen, M. Bursa, A. Eckart, M. Valencia-S, M. Dovčiak, V. Karas, and J. Horák. *MNRAS*, 472:4422–4433, 2017. doi: 10.1093/mnras/stx2312.
- E. P. T. Liang and P. L. Nolan. *Space Sc. Rev.*, 38:353, 1984.
- A. Lichnerowicz. Relativistic hydrodynamics and magnetohydrodynamics: lectures on the existence of solutions. 1967.
- J. F. Lu. *A & A*, 148:176, 1985.
- J. F. Lu. *Gen. Rel. & Grav.*, 18:45L, 1986.

- S. Majumder, S. Nag, and T. K. Das. *MNRAS*, 480(3):3017–3030, 2018. doi: 10.1093/mnras/sty2024.
- D. P. Marrone, J. M. Moran, J. H. Zhao, and R. Rao. *ApJ*, 654:L57–L60, 2007. doi: 10.1086/510850.
- R. Matsumoto, S. Kato, J. Fukue, and A. T. Okazaki. *PASJ*, 36:71, 1984.
- F. Melia. *ApJ*, 387:L25, 1992. doi: 10.1086/186297.
- F. Melia, S. Liu, and R. Coker. *ApJ*, 553:146–157, 2001. doi: 10.1086/320644.
- M. Moscibrodzka. *A & A*, 450(1):93–103, 2006. doi: 10.1051/0004-6361:20054165.
- M. Moscibrodzka, T. K. Das, and B. Czerny. *MNRAS*, 370:219, 2006.
- E. Mossoux and N. Grosso. *A & A*, 604:A85, 2017. doi: 10.1051/0004-6361/201629778.
- E. Mossoux, B. Finociety, J. M. Beckers, and F. H. Vincent. *A & A*, 636:A25, 2020. doi: 10.1051/0004-6361/201937136.
- B. Muchotrzeb and B. Czerny. *Acta Astron.*, 36:1, 1986.
- B. Muchotrzeb and B. Paczynski. *Acta Astron.*, 32:1, 1982.
- H. Nagakura and S. Yamada. *ApJ*, 689:391, 2008.
- H. Nagakura and S. Yamada. *ApJ*, 696:2026, 2009.
- K. Nakayama. *MNRAS*, 281:226, 1996.
- K. Nakayama and J. Fukue. *PASJ*, 41:271, 1989.
- I. Novikov and K. S. Thorne. *Black Holes, ed. De Witt C. & De Witt B.* Gordon and Breach, New York, 1973.
- T. Okuda and D. Molteni. *MNRAS*, 425:2413–2421, Oct 2012. doi: 10.1111/j.1365-2966.2012.21571.x.
- T. Okuda, V. Teresi, E. Toscano, and D. Molteni. *PASJ*, 56(3):547, 2004.
- I. Palit, A. Janiuk, and P. Sukova. *MNRAS*, 487(1):755–768, 2019. doi: 10.1093/mnras/stz1296.
- V. I. Pariev. *MNRAS*, 283:1264, 1996.
- J. Peitz and S. Appl. *MNRAS*, 286:681, 1997.
- R. Penrose and R. M. Floyd. *Nat. Phys. Sc.*, 229(6):177–179, 1971. doi: 10.1038/physci229177a0.
- H. Riffert and H. Herold. *ApJ*, 450:508, 1995.

- S. R. Roberts, Y. F. Jiang, D. Q. Wang, and J. P. Ostriker. *MNRAS*, 466(2):1477–1490, 2017. doi: 10.1093/mnras/stw2995.
- S. Saha, S. Sen, S. Nag, S. Raychowdhury, and T. K. Das. *New Astron.*, 43:10–21, 2016. doi: 10.1016/j.newast.2015.07.007.
- B. Sarkar and S. Das. *Journal of Astrophysics and Astronomy*, 39(1):3, 2018. doi: 10.1007/s12036-017-9503-4.
- M. A. Shaikh. *Class. & Quant. Grav.*, 35(5):055002, 2018. doi: 10.1088/1361-6382/aaa5cd.
- M. A. Shaikh and T. K. Das. *Phys. Rev. D*, 98:123022, 2018. doi: 10.1103/PhysRevD.98.123022.
- M. A. Shaikh, I. Firdousi, and T. K. Das. *Class. & Quant. Grav.*, 34(15):155008, 2017. doi: 10.1088/1361-6382/aa7b19.
- M. A. Shaikh, S. Maity, S. Nag, and T. K. Das. *New Astron.*, 69:48–57, 2019. doi: 10.1016/j.newast.2018.12.001.
- H. Sponholz and D. Molteni. *MNRAS*, 271:233, 1994.
- S. H. Strogatz. *Nonlinear Dynamics And Chaos: With Applications To Physics, Biology, Chemistry, And Engineering*. Westview Press, 2001.
- P. Suková. In *RAGtime 17-19: Workshops on Black Holes and Neutron Stars*, pages 163–176, 2017.
- P. Suková and A. Janiuk. *MNRAS*, 447(2):1565–1579, 2015. doi: 10.1093/mnras/stu2544.
- P. Suková, S. Charzyński, and A. Janiuk. *MNRAS*, 472(4):4327–4342, 2017. doi: 10.1093/mnras/stx2254.
- M. Takahashi. *ApJ*, 570(1):264–276, 2002. doi: 10.1086/339497.
- M. Takahashi, D. Rilett, K. Fukumura, and S. Tsuruta. *ApJ*, 572:950, 1992.
- M. Takahashi, D. Rillet, K. Fukumura, and S. Tsuruta. *ApJ*, 572(2):950–961, 2002. doi: 10.1086/340380.
- M. Takahashi, J. Goto, K. Fukumura, D. Rilett, and S. Tsuruta. *ApJ*, 645:1408, 2006.
- P. Tarafdar and T. K. Das. *New Astron.*, 62:1–14, 2018. doi: 10.1016/j.newast.2017.12.007.
- P. Tarafdar, D. A. Bollimpalli, S. Nag, and T. K. Das. *Phys. Rev. D*, 100:043024, 2019.
- A. H. Taub. *Phys. Rev.*, 74(3):328–334, 1948. doi: 10.1103/PhysRev.74.328.
- A. H. Taub. *Annual Review of Fluid Mechanics*, 10:301–332, 1978.
- K. S. Thorne. *ApJ*, 179:897–908, 1973. doi: 10.1086/151927.

K. S. Thorne. *ApJ*, 191:507–520, 1974. doi: 10.1086/152991.

G. Tóth, R. Keppens, and M. A. Botchev. *A & A*, 332:1159, 1998.

R. X. Yang and M. Kafatos. *A & A*, 295:238, 1995.